Entanglement Hamiltonian of two disjoint blocks in the harmonic chain

OPEN ACCESS

Journal of Statistical Mechanics: Theory and Experiment
An IOP and SISSA journal

PAPER: Quantum statistical physics, condensed matter, integrable systems

Entanglement Hamiltonian of two disjoint blocks in the harmonic chain

Francesco Gentile, Andrei Rotaru* and Erik Tonni

SISSA and INFN Sezione di Trieste, via Bonomea 265, 34136 Trieste, Italy
E-mail: randrei97@gmail.com

Received 8 April 2025
Accepted for publication 11 May 2025
Published 31 July 2025

Online at stacks.iop.org/JSTAT/2025/073102
https://doi.org/10.1088/1742-5468/addaa7

Abstract. We study the entanglement Hamiltonian of two disjoint blocks in the harmonic chain on the line and in its ground state. In the regime of large mass, the only non-vanishing terms are the on-site and nearest-neighbour ones. Analytic expressions are obtained for their profiles, which are written in terms of piecewise linear functions that can be discontinuous and display sharp transitions as the separation between the blocks changes. In the regime of vanishing mass, where the matrices characterizing the entanglement Hamiltonian contain couplings at all distances, we explore the location of the subdominant terms and some combinations of matrix elements that are useful for the continuum limit, comparing the results with the corresponding ones for a free chiral current. The single-particle entanglement spectrum is also investigated.

Keywords: entanglement in extended quantum systems, solvable lattice models

*Author to whom any correspondence should be addressed.

Contents

1. Introduction

The entanglement Hamiltonian is an important operator to investigate in order to understand bipartite entanglement in quantum systems [1–3]. Consider a quantum system in a state characterized by the density matrix ρ whose space is divided into two regions, A

J. Stat. Mech. (2025) 073102

and B. Assuming that its Hilbert space can be factorized accordingly, *i.e.* $\mathcal{H} = \mathcal{H}_A \otimes \mathcal{H}_B$, the reduced density matrix of subsystem A is defined as $\rho_A \equiv \mathrm{Tr}_{\mathcal{H}_B}\rho$, which is a positive, non-singular and self-adjoint operator; hence, it can be written as $\rho_A \equiv \mathrm{e}^{-K_A}$, where K_A is, by definition, the entanglement Hamiltonian for subsystem A. The von Neumann entropy of ρ_A gives the entanglement entropy $S_A \equiv -\mathrm{Tr}_{\mathcal{H}_A}\big(\rho_A \log \rho_A\big)$. When the system is in a pure state (*e.g.* its ground state), ρ is the projector on this state, and the Schmidt decomposition tells us that $S_A = S_B$. It is insightful to study the operator K_A both in lattice models and in quantum field theories, also exploring the continuum limit procedure that relates them.

The first crucial result for entanglement Hamiltonians was obtained by Bisognano and Wichmann [4, 5] within the context of algebraic quantum field theory [1]. Considering a relativistic quantum field theory in the ground state, whose space is bipartite into two equal parts by a hyperplane, they found that K_A is the generator of the boosts along the direction identifying the bipartition. As for lattice models, in a one-dimensional infinite harmonic chain in its ground state, the entanglement Hamiltonian of a half chain was studied through the corner transfer matrix (CTM) in [6, 7], and an operator given by the energy density multiplied by a linear weight function was found, in agreement with the results of Bisognano and Wichmann regarding the continuum limit.

Entanglement Hamiltonians in quantum field theories have been mainly explored for conformal field theories (CFTs) because the symmetry allows various cases to be studied by combining the results of Bisognano and Wichmann and proper conformal mapping. For instance, K_A of the sphere in Minkowski space-time when the entire CFT is in its ground state has been studied [8, 9] for a generic number of space-time dimensions. Instead, since in two-dimensional CFTs the conformal symmetry is infinitely dimensional, more examples can be explored, such as, for example, the case of an interval on a circle when the system is in the ground state, and the case of an interval on a line at a finite temperature [10, 11]. In all these two-dimensional CFT setups, the entanglement Hamiltonian takes the form $K_A = \int_a^b \beta(x)\, T_{tt}(x)\, \mathrm{d}x$; *i.e.* it is a local operator given by the integral over the interval $A = [a, b]$ of the energy density T_{tt} multiplied by the proper weight function $\beta(x)$. Some of these CFT results have also been obtained through lattice computations, mainly in free models, where the properties of Gaussian states can be employed [12–17]. The continuum limit procedure is highly non-trivial because the quadratic operator to consider is inhomogeneous and contains long-range hopping terms. In particular, the continuum limit procedure involves all the diagonals of the matrices characterizing the quadratic operator.

In order to gain insights into the structure of entanglement Hamiltonians, it is important to investigate free massive quantum systems in one spatial dimension bipartite by an interval. The analytic expression of this operator in the continuum limit is not available in the literature, but some studies indicate that it is fully non-local [12, 18–20]. In one-dimensional infinite lattices, the entanglement Hamiltonians of a single block in the massive regime have been explored when the mass parameter takes very large values, both in a harmonic chain and in a free fermionic model, finding that the corresponding matrices significantly simplify in this regime. In particular, they become tridiagonal,

J. Stat. Mech. (2025) 073102

and the inhomogeneity is described by a simple triangular profile [21], whose analytic expression can be constructed from the above-mentioned results for a half chain [6, 7].

Another important class of entanglement Hamiltonians corresponds to a subsystem A made by many disjoint regions. In one spatial dimension, the simplest case is $A = A_1 \cup A_2$, where A_1 and A_2 are two disjoint blocks of contiguous sites in the infinite line. In the continuum, very few entanglement Hamiltonians in this class are available in the literature, and all of them involve non-local terms. For a massless Dirac fermion on the line and in the ground state, when A is the union of two disjoint intervals on the line, K_A is a quadratic operator that also includes a bi-local term [22]. This result has also been recovered from a free fermionic chain through a non-trivial continuum limit procedure [23], along the lines of the method developed for a single block [12, 17]. For a massless Dirac field in the ground state, bi-local terms in entanglement Hamiltonians have also been found in some cases where translation invariance does not occur, such as, for example, when A is either an interval in the half line [24] (see [23] for the corresponding lattice computations) or the union of two disjoint equal intervals at the same distance from a point-like defect on the line [25]. Bi-local terms also occur in the entanglement Hamiltonian of an interval on a circle for a massless Dirac field at a finite temperature [26, 27]. As for the entanglement Hamiltonian of two disjoint intervals on the line for a free bosonic model, the case of a chiral current of a massless scalar field in the ground state has been explored in [28], finding that it contains also fully non-local terms. This model [28–30] is different from a massless scalar field (indeed, it does not, for example, satisfy the Haag duality [28]), and a numerical check of K_A through a lattice computation is not available in the literature.

Further lattice results on entanglement Hamiltonians have been reviewed in [31].

The bipartite entanglement of a one-dimensional quantum system in its ground state when subsystem A is the union of disjoint intervals has been largely explored in the literature through entanglement entropies. These scalar quantities are simpler and easier to evaluate than the corresponding entanglement Hamiltonians; hence, they are sometimes also accessible for more complicated models, such as, for example, some non-trivial CFT models [32–39]. The entanglement entropy of disjoint regions has also been studied in the context of gauge/gravity correspondence through the formula proposed in [40, 41] for the gravitational side of the duality. Interestingly, this quantity displays sharp transitions as the separation distances between the disjoint regions change [42–45]. These transitions provide a characteristic feature of CFT models with holographic duals at strong coupling.

In this article, we perform some numerical analyses of the entanglement Hamiltonian of two disjoint blocks in a harmonic chain on the line and in its ground state. We mainly focus on the two regimes where the mass parameter is either very large or vanishing.

The outline of this article is as follows. In section 2, we describe the setting by defining the harmonic chain in the infinite line, its ground state correlators and the quantities of interest. In section 3, we briefly provide some general features of the entanglement Hamiltonian of two disjoint blocks in massive regimes. The remaining part of the article can be divided into two parts, corresponding to the limiting regimes of large and vanishing masses.

J. Stat. Mech. (2025) 073102

In the first part the large mass regime is explored by first reviewing the existing results about the entanglement Hamiltonian of the half chain and of the single block (section 4) and then discussing our findings about the entanglement Hamiltonian of two disjoint blocks having either equal or unequal lengths (sections 5 and 6, respectively). In this regime of large mass, we extend the results for a single block reported in [21], finding that the matrices characterizing the entanglement Hamiltonian become three-diagonal with inhomogeneity profiles that display sharp transitions as the separation distance changes. In the second part, we report some results for the entanglement Hamiltonians of two generic blocks in the line when the mass parameter is vanishing. In this regime, both a harmonic chain in a massless limit (section 7) and a free chiral current model [28] (section 8) are investigated. Some conclusions are drawn in section 9. Appendices A–F contain technical details and supplementary results supporting the discussions reported in the main text.

2. Entanglement Hamiltonians in an infinite harmonic chain

In this section, we first introduce the model and then report the expressions providing the entanglement Hamiltonian that will be employed throughout our numerical analyses.

The Hamiltonian of the harmonic chain with nearest-neighbour spring-like interaction on an infinite line reads

$$\widehat{H} = \sum_{i\in\mathbb{Z}} \left(\frac{1}{2m}\hat{p}_i^2 + \frac{m\omega^2}{2}\hat{q}_i^2 + \frac{K}{2}(\hat{q}_{i+1}-\hat{q}_i)^2 \right) \tag{2.1}$$

where $\hat{q}_i$ and $\hat{p}_i$ are Hermitean operators satisfying the canonical commutation relations given by $[\hat{q}_i\,,\hat{p}_j] = \mathrm{i}\delta_{i,j}$ and $[\hat{q}_i\,,\hat{q}_j] = [\hat{p}_i\,,\hat{p}_j] = 0$, in units where $\hbar = 1$. The parameters m, K and ω in (2.1) correspond, respectively, to the mass of the oscillators, the nearest-neighbour coupling and the frequency characterizing the confining potential at each site.

A canonical transformation implementing the replacement of $\hat{p}_i$ and $\hat{q}_i$ with $(Km)^{1/4}\hat{p}_i$ and $(Km)^{-1/4}\hat{q}_i$, respectively, leads us to write (2.1) as follows:

$$\widehat{H} = \sqrt{K/m}\sum_{i\in\mathbb{Z}} \frac{1}{2}\left(\hat{p}_i^2 + \frac{\omega^2}{K/m}\hat{q}_i^2 + (\hat{q}_{i+1}-\hat{q}_i)^2 \right) \tag{2.2}$$

where $\sqrt{K/m}$ has the dimension of the energy, in the units where $\hbar = 1$ that we are considering. In (2.2), the positions and momenta are dimensionless, and the frequency is measured in units of $\sqrt{K/m}$. For simplicity, we set $K = m = 1$ throughout our numerical analyses; hence, ω is the only parameter characterizing the Hamiltonian of a harmonic chain on the line. The continuum limit of (2.1) gives the Hamiltonian a massive scalar field, whose massless limit is a prototypical example of a CFT with central charge $c = 1$.

In our analyses, we focus on the ground state of a harmonic chain on the line, which is fully characterized by the corresponding correlation functions for the positions and momenta, which are given, respectively, by

J. Stat. Mech. (2025) 073102

$$\langle \hat{q}_i \, \hat{q}_j \rangle = \int_{-\pi}^{+\pi} \frac{\cos\left[q\,(i-j)\right]}{\sqrt{\omega^2 + 4\left[\sin\left(q/2\right)\right]^2}} \, \frac{\mathrm{d}q}{4\pi} \tag{2.3}$$

$$\langle \hat{p}_i \, \hat{p}_j \rangle = \int_{-\pi}^{+\pi} \sqrt{\omega^2 + 4\left[\sin\left(q/2\right)\right]^2} \, \cos\left[q\,(i-j)\right] \, \frac{\mathrm{d}q}{4\pi} \, . \tag{2.4}$$

These expressions can be equivalently written as integrals over $q \in (0, 2\pi)$ by first splitting the integration domain as $(-\pi, 0] \cup [0, \pi)$ and then redefining the integration variable as $\tilde{q} = q + 2\pi$ when $q \in (-\pi, 0]$. Calculating the integrals in (2.3) and (2.4), one finds, respectively, [46]

$$\langle \hat{q}_i \, \hat{q}_{i+r} \rangle = \frac{\kappa^{r+1/2}}{2} \, \frac{\Gamma\left(r + 1/2\right)}{\Gamma\left(1/2\right) \, \Gamma\left(r+1\right)} \, {}_2F_1\left(1/2, r+1/2; r+1; \kappa^2\right) \tag{2.5}$$

$$\langle \hat{p}_i \, \hat{p}_{i+r} \rangle = \frac{\kappa^{r-1/2}}{2} \, \frac{\Gamma\left(r - 1/2\right)}{\Gamma\left(-1/2\right) \, \Gamma\left(r+1\right)} \, {}_2F_1\left(-1/2, r-1/2; r+1; \kappa^2\right) \tag{2.6}$$

where ${}_2F_1$ is the hypergeometric function, and the parameter κ is defined as

$$\kappa \equiv \frac{\left(\sqrt{\omega^2+4} - \omega\right)^2}{4} \tag{2.7}$$

which satisfies $0 < \kappa < 1$. The correlators (2.5) and (2.6) provide the generic elements of the correlation matrices Q and P, respectively. These matrices allow us to construct the covariance matrix $\gamma \equiv Q \oplus P$, which fully characterizes the ground state of this system. We remark that the translation invariance of the model induces the occurrence of a zero mode, which prevents us from setting $\omega = 0$; indeed, the correlator (2.3) is divergent in this case.

Consider a bipartition of the chain given by subsystem A and its complement B, where A is the union of disjoint blocks of contiguous sites. This leads to the natural assumption that, correspondingly, the Hilbert space can be written as $\mathcal{H} = \mathcal{H}_A \otimes \mathcal{H}_B$. Since we are considering the ground state of the harmonic chain (2.1), the reduced density matrix $\rho_A \equiv \mathrm{Tr}_{\mathcal{H}_B}(|0\rangle\langle 0|)$ of subsystem A remains Gaussian.

The bipartite entanglement associated with this bipartition of the harmonic chain in its ground state [2, 3, 46–53] can be studied by constructing the reduced covariance matrix $\gamma_A \equiv Q_A \oplus P_A$, where Q_A and P_A are the correlation matrices reduced to subsystem A, whose generic element is given by $(Q_A)_{i,j} \equiv Q_{i,j}$ and $(P_A)_{i,j} \equiv P_{i,j}$, respectively, where $i, j \in A$; hence, γ_A is a $(2L_A) \times (2L_A)$ matrix, where L_A is the number of sites in A. Since the reduced covariance matrix γ_A is real, symmetric and positive definite, its Williamson decomposition provides the symplectic spectrum $\{\sigma_k \, ; 1 \leqslant k \leqslant L_A\}$ of γ_A, which can be obtained from the eigenvalues of $Q_A P_A$ in a standard way for the cases explored in our analyses.

The Rényi entropies $S_A^{(n)}$ and the entanglement entropy S_A are scalar quantities that are defined, respectively, as $S_A^{(n)} \equiv \frac{1}{1-n} \log\left(\mathrm{Tr}\rho_A^n\right)$ and $S_A \equiv -\mathrm{Tr}(\rho_A \log \rho_A) = \lim_{n \to 1} S_A^{(n)}$,

J. Stat. Mech. (2025) 073102

in terms of ρ_A. For the case we are considering, these entanglement quantifiers can be obtained from the symplectic spectrum of γ_A as follows:

$$S_A^{(n)} = \frac{1}{n-1} \sum_{k=1}^{L_A} \log[(\sigma_k + 1/2)^n - (\sigma_k - 1/2)^n] \tag{2.8}$$

$$S_A = \sum_{k=1}^{L_A} [(\sigma_k + 1/2) \log(\sigma_k + 1/2) - (\sigma_k - 1/2) \log(\sigma_k - 1/2)] \,. \tag{2.9}$$

Since the reduced density matrix $\rho_A = \mathrm{e}^{-K_A}$ is Gaussian, the corresponding entanglement Hamiltonian K_A is a quadratic operator [3]

$$\widehat{K}_A = \frac{1}{2} \sum_{i,j \in A} (T_{i,j}\, \hat{p}_i\, \hat{p}_j + V_{i,j}\, \hat{q}_i\, \hat{q}_j) = \frac{1}{2}\, \hat{\boldsymbol{r}}^{\mathrm{t}} H_A\, \hat{\boldsymbol{r}} \qquad \hat{\boldsymbol{r}} \equiv \begin{pmatrix} \hat{\boldsymbol{q}} \\ \hat{\boldsymbol{p}} \end{pmatrix} \tag{2.10}$$

where the $(2L_A) \times (2L_A)$ symmetric matrix $H_A = V \oplus T$ is block diagonal, and the $L_A \times L_A$ symmetric matrices T and V correspond to the kinetic and potential energy terms, whose explicit expression in terms of the reduced correlation matrices Q_A and P_A read, respectively, as

$$V = h\left(\sqrt{P_A Q_A}\right) P_A = P_A\, h\left(\sqrt{Q_A P_A}\right) \tag{2.11}$$

$$T = h\left(\sqrt{Q_A P_A}\right) Q_A = Q_A\, h\left(\sqrt{P_A Q_A}\right) \tag{2.12}$$

with $h(y)$ being the function defined as follows:

$$h(y) \equiv \frac{1}{y} \log\left(\frac{y + 1/2}{y - 1/2}\right). \tag{2.13}$$

The expressions (2.10)–(2.13) have been employed in various analyses (see *e.g.* [12, 21, 54–56]).

The entanglement Hamiltonian (2.10) can be written as $\widehat{K}_A = \frac{1}{2} \sum_{k=1}^{L_A} \varepsilon_k \hat{f}_k^\dagger \hat{f}_k$, where f_k are the proper bosonic operators, and ε_k are the single-particle entanglement energies, which can be found from the symplectic eigenvalues of γ_A as [7]

$$\varepsilon_k = 2\, \mathrm{arccoth}\,(2\sigma_k) = \log\left(\frac{\sigma_k + 1/2}{\sigma_k - 1/2}\right) \tag{2.14}$$

which can be inverted, finding $\sigma_k = \frac{1}{2} \coth(\varepsilon_k/2)$. The single-particle entanglement spectrum, whose elements are (2.14), has been largely discussed in the literature [2].

In the case mainly considered in this article, the bipartition of the line is given by the union of the blocks A_1 and A_2, made by L_1 and L_2 sites, respectively, separated

J. Stat. Mech. (2025) 073102

by D sites; hence, the subsystem $A = A_1 \cup A_2$ contains $L_A = L_1 + L_2$ sites. We find it convenient to introduce the dimensionless parameter

$$\delta \equiv \frac{D}{L_A} \tag{2.15}$$

corresponding to the separation distance, and the dimensionless parameter characterizing the relative size of the two blocks

$$\rho \equiv \frac{L_1}{L_A} = \frac{1}{1+\chi} \qquad \Longleftrightarrow \qquad \chi \equiv \frac{L_2}{L_1} = \frac{1-\rho}{\rho}\,. \tag{2.16}$$

Since $L_1 \leqslant L_2$ can be assumed without loss of generality, $\rho \in (0, 1/2]$ and $\chi \geqslant 1$ hereafter.

Throughout this article, the indices i and j label the physical sites in the subsystem $A = A_1 \cup A_2$ (see *e.g.* (2.10)). Considering the index $\tilde{i} \in [1, L_A]$ labelling either the rows or the columns of the $L_A \times L_A$ matrices in (2.11) and (2.12), the relation between i and $\tilde{i}$ depends on the choice of the origin for the index i in the chain. For instance, taking the origin as the first endpoint of A_1, we have

$$\begin{cases} i = \tilde{i} & i \in A_1 \qquad \tilde{i} \in [1, L_1] \\ i = \tilde{i} + D & i \in A_2 \qquad \tilde{i} \in [L_1 + 1, L_1 + L_2]\,. \end{cases} \tag{2.17}$$

Since both the sizes of the blocks and their separation distances are even in our analyses, a natural choice for the origin is the middle of the finite block separating A_1 and A_2. This gives

$$\begin{cases} i = \tilde{i} - L_1 - \lfloor D/2 \rfloor & i \in A_1 \qquad \tilde{i} \in [1, L_1] \\ i = \tilde{i} - L_1 + \lfloor (D+1)/2 \rfloor & i \in A_2 \qquad \tilde{i} \in [L_1 + 1, L_1 + L_2] \end{cases} \tag{2.18}$$

where $\lfloor \ldots \rfloor$ denotes the floor function.

3. Massive regime

In this section, we briefly discuss some numerical results for matrices T and V characterizing the entanglement Hamiltonian (2.10) in an infinite harmonic chain in its ground state, evaluated through the expressions (2.11)–(2.13), when the subsystem $A = A_1 \cup A_2$ is made by the union of two disjoint blocks (see section 2), and the mass parameter ω is finite and does not take extreme values.

Since subsystem A is the union of the two blocks A_1 and A_2, it is natural to introduce the block decomposition of T and V provided by such bipartition of A, namely

$$T = \left(\begin{array}{c|c} T^{(1,1)} & T^{(1,2)} \\ \hline T^{(2,1)} & T^{(2,2)} \end{array}\right) \qquad V = \left(\begin{array}{c|c} V^{(1,1)} & V^{(1,2)} \\ \hline V^{(2,1)} & V^{(2,2)} \end{array}\right) \tag{3.1}$$

where the diagonal blocks correspond to the sites in A_1 and A_2 (hence they are $L_1 \times L_1$ and $L_2 \times L_2$ symmetric matrices, respectively), and the off-diagonal blocks of T and V

J. Stat. Mech. (2025) 073102

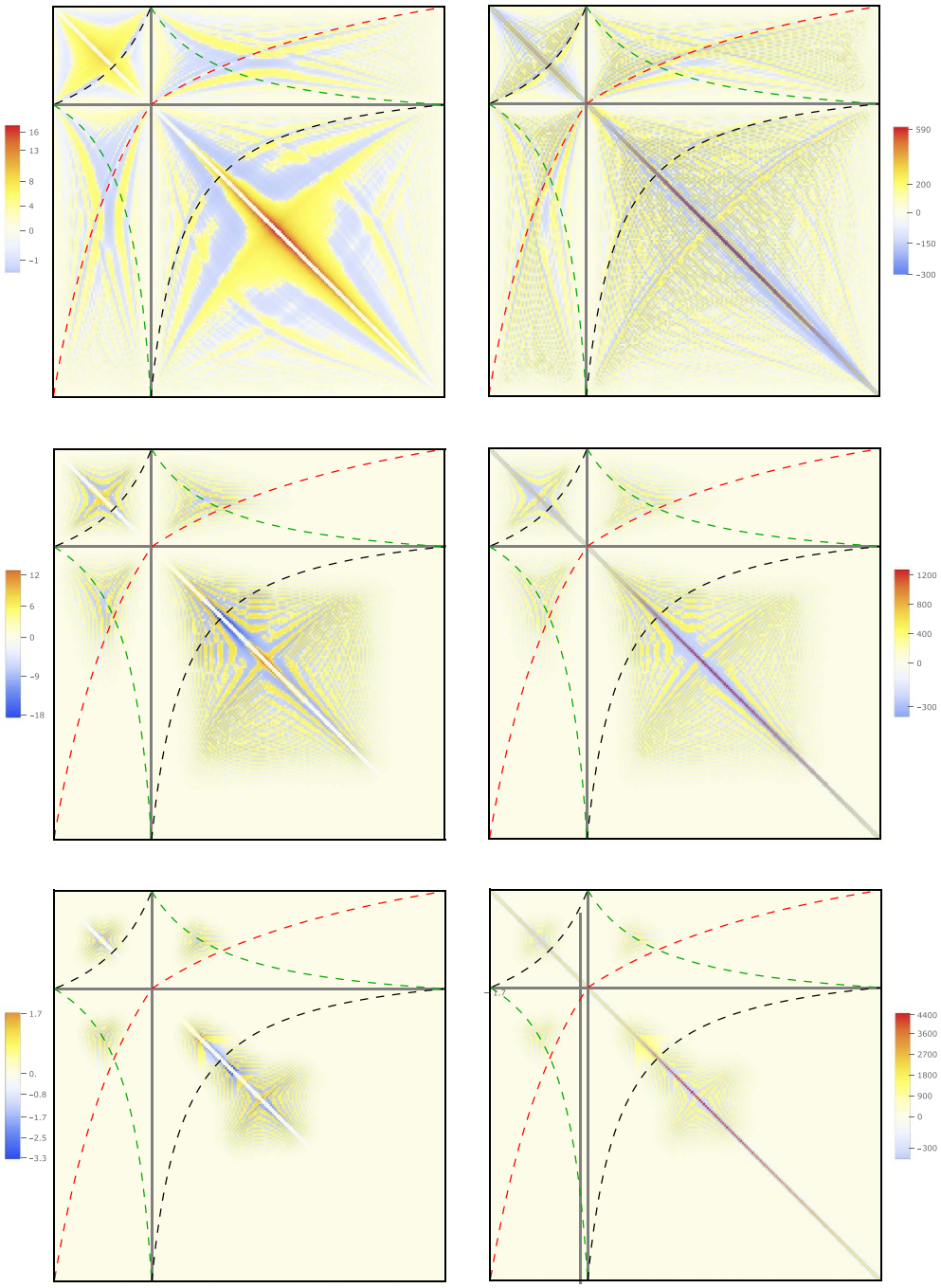

Figure 1. Matrix T (left) and V (right) in the massive regime with either $\omega = 0.1$ (top), $\omega = 1$ (middle) or $\omega = 3$ (bottom) for $L_2 = 3L_1$ with $L_1 = 50$ and $\delta = 1/4$.

are rectangular matrices whose elements are identified by one site in A_1 and the other one in A_2. In figure 1, the block decomposition (3.1) is given by the grey straight lines.

In figure 1, we show matrices T (left panels) and V (right panels) for increasing values of the mass parameter $\omega \in \{0.1, 1, 3\}$, going from the top to the bottom panels.

J. Stat. Mech. (2025) 073102

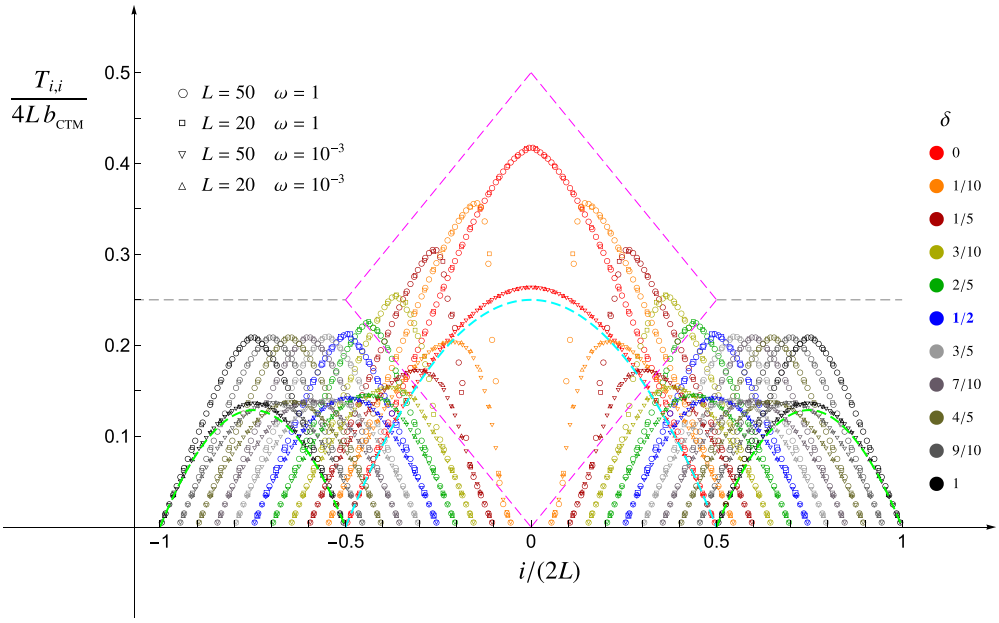

Figure 2. Main diagonal of T for two equal blocks made by L sites when $\omega = 1$ and $\omega = 10^{-3}$ for various values of δ (see (2.15)). The magenta and grey dashed segments refer to a large ω regime (see figure 4), while the green and cyan dashed lines correspond to a massless regime (see *e.g.* figures 18 and 34).

The blocks A_1 and A_2 contain $L_1 = 50$ and $L_2 = 150$ sites, respectively, and are separated by $D = 50$ sites. The main diagonal and the two next to it of the matrix T provide the largest amplitudes; hence, in the left panels of figure 1, these three diagonals have been removed, in order to make visible the remaining elements of the matrix.

Some plots of these matrices in the massive regime have also been shown in [12]. The main feature to highlight about these matrices is their non-local and inhomogeneous nature. Since finding analytic results about matrices T and V for this bipartition in a massive regime is extremely difficult, in this article we mainly focus on the limiting regimes of large ω (see sections 5 and 6) and vanishing ω (see section 7). The dashed curves in figure 1 correspond to analytic curves occurring in a massless regime and will be introduced in section 7.

It is worth remarking that, in figure 1, the matrix elements corresponding to non-local terms vanish as ω increases and that a local operator is obtained in the extreme regime where $\omega \gg 1$. In the limit of large ω, matrices T and V become three-diagonal; hence, they are fully described by simple profiles. These functions, which have been discussed in [21] for the case of a single block, will be investigated in sections 5 and 6 for the case of the union of two disjoint blocks.

In figure 2, we consider blocks of equal length and show the main diagonal of T for either $\omega = 1$ or $\omega = 10^{-3}$ (the constant $b_{\rm CTM}$ depends on ω and is introduced below, in (4.3)). The data points in figure 2 obtained for $\omega = 1$ should be combined with those displayed in the middle panels of figure 1. Nice collapses are observed for the data sets corresponding to different values of L, and it would be very interesting to find analytic

J. Stat. Mech. (2025) 073102

expressions for these curves. A similar result was found for the main diagonal of V, but we have not reported it here. In this figure, the grey and magenta dashed straight lines provide the structure obtained in the large ω regime and described in section 5 (these curves are also displayed in figure 4), while the cyan and green dashed curves correspond to the opposite limiting regime $\omega \to 0^+$, for vanishing and large separation distances, respectively (*e.g.* in the top panel of figure 34, see the black dashed curve for $\delta = 0$ and the solid green curves, respectively).

Our numerical analyses are based on the matrices (2.11) and (2.12). The main technical difficulty in our numerical analyses is that high precision is required. This is needed because, whenever a symplectic eigenvalue is very close to $(1/2)^+$, it is approximated to $1/2$ by the software (Mathematica, in our case); but this is forbidden because it corresponds to a singularity in (2.14). In order to avoid this approximation, very high precision is needed. This crucial technical issue has already been highlighted in various works on entanglement Hamiltonians in harmonic lattices [12, 15, 16, 21, 56]. In particular, the numerical results reported in figures 1 and 2 have been obtained by using 2000 significant digits.

4. Large ω regime: half chain and single block

Considering the ground state of a harmonic chain (2.1), in this section we review the analytic results for the entanglement Hamiltonian (2.10) of a half chain [6, 7] and of a single block the regime of large mass [21].

The entanglement Hamiltonian (2.10) when subsystem A is a half chain with sites $i \in [1, +\infty)$ has been investigated in [7], through the CTM technique developed in [6]. In the regime of large ω, matrices T and V become diagonal and tri-diagonal, respectively (see also [21]). Their non-vanishing elements are described well by

$$T_{i,i} = 2b_{\text{CTM}}\,(i - 1/2) \tag{4.1}$$

and

$$V_{i,i} = \left(\omega^2 + 2\right) 2b_{\text{CTM}}\,(i - 1/2) \qquad\qquad V_{i,i+1} = -\,2b_{\text{CTM}}\,i \tag{4.2}$$

where $i \geqslant 1$, and the coefficient b_{CTM} depends on ω, as follows:

$$b_{\text{CTM}} \equiv 2\sqrt{\kappa}\,I\,(\kappa') \qquad\qquad \kappa' \equiv \sqrt{1-\kappa^2} \tag{4.3}$$

being κ defined as in (2.7), and $I(y)$ is the complete elliptic integral of the first kind. In this setup, the single-particle entanglement spectrum is given by [7]

$$\varepsilon_k = 2\varepsilon_{\text{CTM}}\,(k - 1/2) \qquad\qquad \varepsilon_{\text{CTM}} \equiv \pi\,\frac{I\,(\kappa')}{I\,(\kappa)} \qquad\qquad k \geqslant 1\,. \tag{4.4}$$

We remark that, in the massless limit $\omega \to 0$, we have

$$b_{\text{CTM}} \to \pi \qquad\qquad \varepsilon_{\text{CTM}} \to 0 \tag{4.5}$$

for the expressions introduced in (4.3) and (4.4), respectively.

The entanglement Hamiltonian (2.10) when A is a block made by L sites in an infinite chain has been studied in [21], finding that, in the regime of large ω, the matrices T and V become diagonal and tridiagonal, respectively, also in this case. The profiles characterizing the non-vanishing diagonals are (see figure 3 of [21])

$$\frac{T_{i,i}}{L} = 2b_{\text{CTM}}\, F_1\!\left(\frac{i-1/2}{L}\right) \tag{4.6}$$

and

$$\frac{V_{i,i}}{L} = \left(\omega^2+2\right) 2b_{\text{CTM}}\, F_1\!\left(\frac{i-1/2}{L}\right) \qquad\qquad \frac{V_{i,i+1}}{L} = -\,2b_{\text{CTM}}\, F_1\!\left(\frac{i}{L}\right) \tag{4.7}$$

where $1 \leqslant i \leqslant L$, the coefficient b_{CTM} is given in (4.3) and the function $F_1(x)$ can be introduced through $\Delta(a,b;x)$, a continuous function with a triangular shape defined as follows for $x \in \mathbb{R}$:

$$\Delta\left(a,b;x\right) \equiv \Theta_{[a,b]}\left(x\right)\left(\frac{b-a}{2} - \left|x - \frac{a+b}{2}\right|\right) = \begin{cases} x-a & x \in \left[a, \frac{a+b}{2}\right] \\ b-x & x \in \left[\frac{a+b}{2}, b\right] \\ 0 & x \notin [a,b] \end{cases} \tag{4.8}$$

in terms of the characteristic function $\Theta_{[a,b]}(x)$ for the interval $[a,b]$. Setting the origin of the spatial coordinate either in the middle point of A or in its first endpoint, the function $F_1(x)$ to employ in (4.6) and (4.7) reads, respectively,

$$F_1\left(x\right) \equiv \Delta\left(-1/2, 1/2; x\right) \qquad\qquad F_1\left(x\right) \equiv \Delta\left(0, 1; x\right). \tag{4.9}$$

We remark that (4.1) and (4.2) can be obtained by replacing the function $F_1(x)$ with the function x in (4.6) and (4.7), respectively. Further progress about the entanglement Hamiltonian of a single block in a large ω regime has recently been made in [57].

In the same regime of large ω, the single-particle entanglement spectrum for this setup is approximated well by the following linear behaviour [21]:

$$\frac{\varepsilon_k}{L} = 2\varepsilon_{\text{CTM}}\,\frac{k-1/2}{L} \tag{4.10}$$

where $1 \leqslant k \leqslant L$, whose slope is determined by (4.4), as shown in figure 4 of [21].

J. Stat. Mech. (2025) 073102

By employing the single-particle entanglement spectrum for a half line given in (4.4), it has been found that the entanglement entropy at large ω reads [21]

$$S_A = -\frac{1}{12}\left[\log\left(\frac{16\,\kappa'^4}{\kappa^2}\right) - \left(1+\kappa^2\right)\frac{4\,I\left(\kappa\right)I\left(\kappa'\right)}{\pi}\right] \tag{4.11}$$

which is independent of L, as expected from the area law.

5. Large ω regime: two equal blocks

In this section, we explore the entanglement Hamiltonian (2.10) for a harmonic chain in its ground state, in the case where the subsystem $A = A_1 \cup A_2$ is the union of two disjoint blocks and ω is very large. This analysis extends the result obtained in [21] in this regime for a single block, which is reviewed in section 4. In this section, we focus on configurations with equal blocks, *i.e.* $L_1 = L_2 \equiv L$, implying that (2.15) becomes $\delta = D/(2L)$, while the case $L_1 \neq L_2$ is investigated in section 6.

5.1. Entanglement Hamiltonian

In the regime of large ω that we are considering, when $\delta = 0$, the result for a single block given by (4.6) and (4.7) with L replaced by $2L$ must be obtained. Instead, in the opposite regime where δ is sufficiently large, the two blocks become independent, and therefore we expect to find (4.6) and (4.7) for each block. It is worth exploring the interpolation between these two regimes by studying the entanglement Hamiltonian (2.10) for δ that varies between $\delta = 0$ and values such that A_1 and A_2 become independent.

When ω is large enough, one observes that the non-vanishing elements of the matrices (2.11) and (2.12) occurring in the entanglement Hamiltonian (2.10) follow the same three-diagonals approximation found in [21] for a single block, but the profiles along the diagonals now encode the spatial configuration of the bipartition that we are considering. In the special case where the two disjoint blocks have the same size, we find that these non-vanishing diagonals are nicely described by

$$\frac{T_{i,i}}{2L} = 2b_{\text{CTM}}\,\widetilde{F}_2\left(\delta\,;\frac{i-1/2}{2L}\right) \tag{5.1}$$

and

$$\frac{V_{i,i}}{2L} = \left(\omega^2+2\right)2b_{\text{CTM}}\,\widetilde{F}_2\left(\delta\,;\frac{i-1/2}{2L}\right) \qquad \frac{V_{i,i+1}}{2L} = -2b_{\text{CTM}}\,\widetilde{F}_2\left(\delta\,;\frac{i}{2L}\right) \tag{5.2}$$

in terms of the coefficient b_{CTM} defined in (4.3) and the function $\widetilde{F}_2(\delta;x)$ with $x \in [0,1]$, parameterized by $\delta = D/(2L)$. We remark that the index i in (5.1) and (5.2) labels the physical sites (see (2.18)). Notice that (5.1) and (5.2) have the same form of the corresponding quantities for the single block and for half the chain, reported in (4.6), (4.7), (4.1) and (4.2), respectively. The crucial difference is given by the function $\widetilde{F}_2(\delta;x)$.

J. Stat. Mech. (2025) 073102

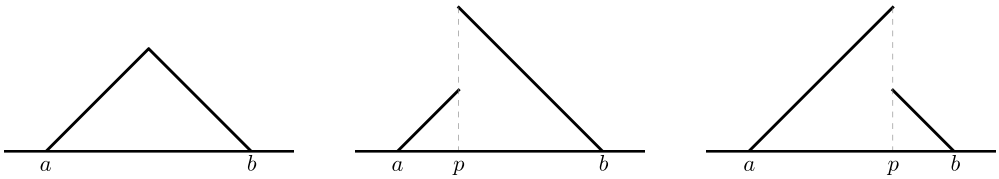

Figure 3. The function (5.3) for $p = \frac{a+b}{2}$ (left), $p < \frac{a+b}{2}$ (middle) and $p > \frac{a+b}{2}$ (right).

In order to define the function $\widetilde{F}_2(\delta;x)$ in (5.1) and (5.2), let us introduce the following auxiliary function:

$$\lambda(a,b;p;x) \equiv \begin{cases} x-a & x\in[a,p] \\ b-x & x\in[p,b] \end{cases} \qquad p\in[a,b] \tag{5.3}$$

which is a real function of $x\in\mathbb{R}$ with support in the interval $\big[a,b\big]$. For a generic $p\in(a,b)$, the function (5.3) is discontinuous at $x=p$, and its name has been chosen because its shape resembles the form of the Greek letter λ when $p<\frac{a+b}{2}$. For $p=\frac{a+b}{2}$, the function (5.3) becomes the continuous triangular function (4.8). In figure 3, the function (5.3) is shown for the three relevant regimes of its parameter p.

The function $\widetilde{F}_2(\delta;x)$ occurring in (5.1) and (5.2) can be written through the functions defined in (4.8) and (5.3) as follows:

$$\widetilde{F}_2(\delta;x) \equiv \begin{cases} \Delta_1(x)+\Delta_2(x) & \delta\geqslant\delta_c \\ \lambda_1(b_1-s(\delta);x)+\lambda_2(a_2+s(\delta);x) & \delta\leqslant\delta_c \end{cases} \tag{5.4}$$

where $b_1-a_1=b_2-a_2=L$, and we have introduced the notation $\Delta_j(x)\equiv\Delta(a_j,b_j;x)$ and $\lambda_j(p;x)\equiv\lambda(a_j,b_j;p;x)$ to enlighten the formula and highlight the fact that the first and the second term in the right-hand side (RHS) correspond to A_1 and A_2, respectively (the dimensionless parameters $a_j<b_j$ refer to the endpoints of the interval A_j). To match the above-mentioned expectations in the two limiting regimes of vanishing and large separation distance $s(\delta)$ in (5.4) must satisfy $s(0)=0$ and $s(\delta)\to 1/4$ as $\delta\to+\infty$, respectively. The function $s(\delta)$ in (5.4) fulfilling these consistency conditions and that nicely fits our numerical data reads

$$s(\delta) \equiv \begin{cases} \delta/2 & \delta\leqslant\delta_c \\ 1/4 & \delta\geqslant\delta_c \end{cases} \tag{5.5}$$

where the critical value of δ corresponds to

$$\delta_c = \frac{1}{2}. \tag{5.6}$$

In figure 4, we report some numerical data points for the main diagonal of T for various values of the parameter δ (obtained through (2.12)), showing that they are described well by the function (5.1), given by the solid curves. The same analysis has been carried out for $V_{i,i}$ and $V_{i,i+1}$ by employing (2.11) for the numerical data points and (5.2) for the

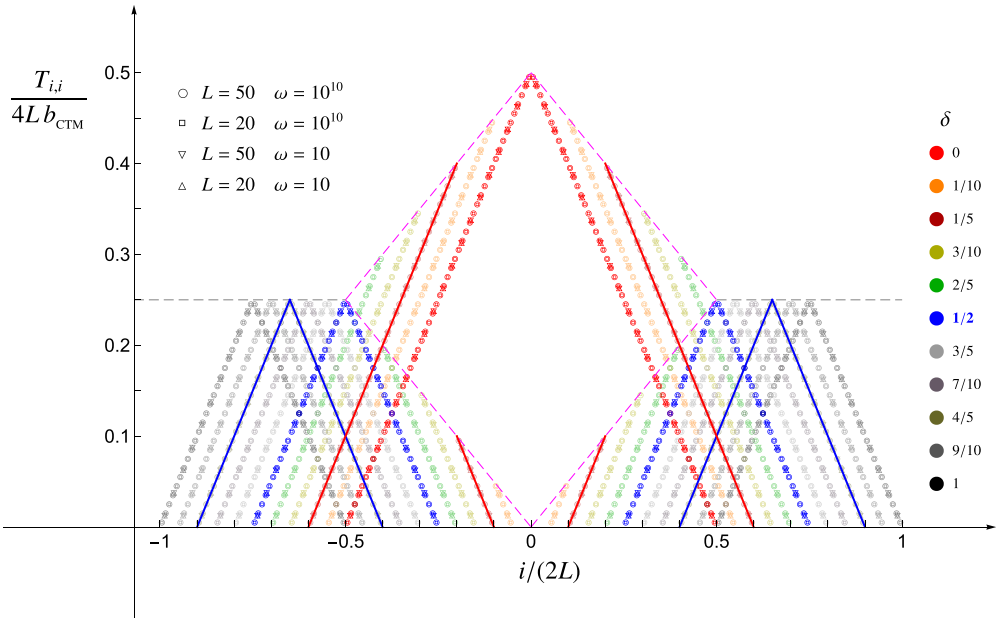

Figure 4. Main diagonal of T for two equal blocks made by L sites in the regime of large ω for various values of δ. The solid curves correspond to the analytic expression in (5.1) (see also (5.4) or (5.7)), which has a sharp transition at the critical value (5.6) (blue data points).

analytic curve. The results are not reported here because they are qualitatively identical to those in figure 4.

A heuristic picture explaining the critical value (5.6) is described in section 6.3.

The expression (5.4) highlights the fact that a transition occurs at the critical value (5.6). An equivalent form for (5.4), just in terms of $s(\delta)$ introduced in (5.5), reads

$$\widetilde{F}_2(\delta;x) \equiv \lambda(a_1,b_1;b_1-s(\delta);x)+\lambda(a_2,b_2;a_2+s(\delta);x)\,. \tag{5.7}$$

Summarising, the function $\widetilde{F}_2(\delta;x)$ introduced in (5.4) or in (5.7) displays two phases separated by the critical value (5.6) for the dimensionless ratio δ. Correspondingly, qualitatively different shapes are observed for the diagonals in (5.1) and (5.2), which are described by two equal triangles when $\delta \geqslant \delta_{\rm c}$ (see the left panel in figure 3) and by two discontinuous piecewise linear functions when $\delta \leqslant \delta_{\rm c}$ (see the middle and right panels in figure 3).

We remark that the specific expression for $s(\delta)$ given by (5.5) and (5.6) cannot be determined just by imposing the asymptotic behaviours at $\delta = 0$ and $\delta \to +\infty$ (see the text above (5.5)). Indeed, for instance, let us consider the following one-parameter family of functions:

$$s\left(\tilde{\delta}_{\rm c};\delta\right) \equiv \begin{cases} \delta/\left(4\tilde{\delta}_{\rm c}\right) & \delta \leqslant \tilde{\delta}_{\rm c} \\ 1/4 & \delta \geqslant \tilde{\delta}_{\rm c} \end{cases} \tag{5.8}$$

J. Stat. Mech. (2025) 073102

which becomes $s(\delta)$ in (5.5) and (5.6) when $\tilde{\delta}_{\rm c}=1/2$. By replacing $s(\delta)$ with $s\big(\tilde{\delta}_{\rm c};\delta\big)$ in (5.4) and (5.7), the resulting $\widetilde{F}_2(\delta;x)$ satisfy the same asymptotic behaviours at $\delta=0$ and $\delta\to+\infty$ for any finite value of the parameter $\tilde{\delta}_{\rm c}$. However, since it displays the transition at $\delta=\tilde{\delta}_{\rm c}$, it disagrees with the numerical data points for $\tilde{\delta}_{\rm c}\neq 1/2$.

In order to compare the analytic expression in (5.4) and (5.7) against the corresponding numerical data, a choice of the endpoints of blocks A_1 and A_2 of equal length is needed.

A convenient choice for the parameters providing the endpoints of the blocks in (5.4) and (5.7) reads

$$a_1=-\frac{\delta}{2}-\frac{1}{2}\qquad b_1=-\frac{\delta}{2}\qquad\qquad a_2=\frac{\delta}{2}\qquad b_2=\frac{\delta}{2}+\frac{1}{2}\tag{5.9}$$

which tells us that the two blocks A_1 and A_2 behave in the same way, symmetrically with respect to the origin, as δ decreases and become adjacent at the origin when $\delta=0$. Setting (5.9) into (5.7), one finds that the asymptotic behaviours of $\widetilde{F}_2(\delta;x)$ in the limiting regimes of vanishing and large separation between the two blocks can be written in terms of (4.8), respectively, as

$$\lim_{\delta\to 0}\widetilde{F}_2\left(\delta;x\right)=\Delta\left(-\frac{1}{2},\frac{1}{2};x\right)\qquad\lim_{\delta\to+\infty}\widetilde{F}_2\left(\delta;x\right)=\Delta\left(-\frac{\delta}{2}-\frac{1}{2},-\frac{\delta}{2};x\right)+\Delta\left(\frac{\delta}{2},\frac{\delta}{2}+\frac{1}{2};x\right).\tag{5.10}$$

A different choice for the parameters determining the endpoints of the blocks in (5.4) and (5.7) corresponds to keep *e.g.* A_1 fixed, namely to choose its endpoints independent of δ. If the origin coincides with the first endpoint of A_1, this parametrization is given by

$$a_1=0\qquad b_1=\frac{1}{2}\qquad\qquad a_2=\frac{1}{2}+\delta\qquad b_2=\delta+1\,.\tag{5.11}$$

When (5.11) is imposed in (5.7), the asymptotic behaviours of $\widetilde{F}_2(\delta;x)$ for vanishing and large separation between the two blocks become, respectively,

$$\lim_{\delta\to 0}\widetilde{F}_2\left(\delta;x\right)=\Delta\left(0,1;x\right)\qquad\lim_{\delta\to+\infty}\widetilde{F}_2\left(\delta;x\right)=\Delta\left(0,1/2;x\right)+\Delta\left(1/2+\delta,1+\delta;x\right).\tag{5.12}$$

As for the numerical precision adopted in these analyses, the numerical results corresponding to $\omega\in\{10,10^2\}$ and $\omega=10^{10}$ have been obtained by employing 3000 and 5000 digits, respectively.

In figure 4, we report some numerical results for $T_{i,i}$ in the regime of large ω for blocks made by $L\in\{20,50\}$ sites and various values of δ. Our analysis shows that $\omega=10^2$ can already be considered a large value for ω in this setup. However, the data for $\omega=10^{10}$ has also been reported, for consistency with the corresponding analyses involving unequal blocks (see section 6), where larger values for ω are required to get a stable picture (see

J. Stat. Mech. (2025) 073102

the discussion of figure 8). Notice that, in figure 4, the parametrization of the endpoints given by (5.9) has been chosen.

The numerical results in figure 4 strongly support the validity of (5.1); indeed, the solid curves correspond to the analytic expression (5.4) or (5.7), with the choice (5.9). In figure 4, we have reported the analytic curve for a typical value $\delta < \delta_c$ and for another typical value $\delta > \delta_c$ (see the solid red and blue curves, respectively), but it has also been checked that the data sets corresponding to the other values of δ in the figure are also nicely reproduced by the analytic expression mentioned above. As already mentioned below (5.6), in the same setup, we have checked that the corresponding numerical results for the matrix V satisfy (5.2) and agree well with the analytic expression of $\widetilde{F}_2(\delta;x)$ in the same way. In figure 4, we have highlighted the blue and the red markers because they correspond, respectively, to the critical value of δ (see (5.6)), where the transition between the two phases occurs, and to $\delta = 0$, *i.e.* to adjacent intervals. The grey and magenta dashed straight lines indicate the interpolation of the relevant vertices as δ varies. These straight lines are also shown in figure 2 as a reference for the large ω regime. The slopes of the solid lines and of the magenta dashed lines in figure 4 are ± 1 and $\pm 1/2$, respectively. Thus, this figure also shows that the expectations mentioned at the beginning of this subsection are fulfilled.

It is insightful to compare figure 4 against figure 2, where the same setups have been considered for different regimes of ω. From this comparison, one observes that the sharp transitions in δ and discontinuous profiles for $\delta < \delta_c$ are characteristic features of the large ω regime. Indeed, they do not occur in figure 2, where smaller values of ω are considered. However, let us remark that the three-diagonal approximation does not hold for the data points reported in figure 2 (see *e.g.* the middle panels of figure 1 for $\omega = 1$).

5.2. Single-particle entanglement spectrum

We find it worth exploring the effect of the occurrence of the two phases described in section 5.1 on the single-particle entanglement spectrum, which is obtained from the symplectic spectrum of the reduced covariance matrix through (2.14), with $1 \leqslant k \leqslant 2L$ in this case.

The numerical results for the single-particle entanglement spectrum are displayed in figure 5 for the same setup as figure 4. These numerical data points are described well by the following analytic expression:

$$\frac{\varepsilon_k}{2L} = \varepsilon_{\text{CTM}}\, \tilde{f}_2\left(\delta\,; \frac{k}{2L}\right) \tag{5.13}$$

where ε_{CTM} has been introduced (4.4) and $\tilde{f}_2(\delta;\eta)$ is a continuous piecewise linear function defined as follows:

$$\tilde{f}_2\,(\delta;\eta) \equiv \begin{cases} \eta/2 & \eta \leqslant \eta_c\,(\delta) \\ \eta - \eta_c\,(\delta)\,/2 & \eta > \eta_c\,(\delta) \end{cases} \qquad \eta \in [0,1] \tag{5.14}$$

J. Stat. Mech. (2025) 073102

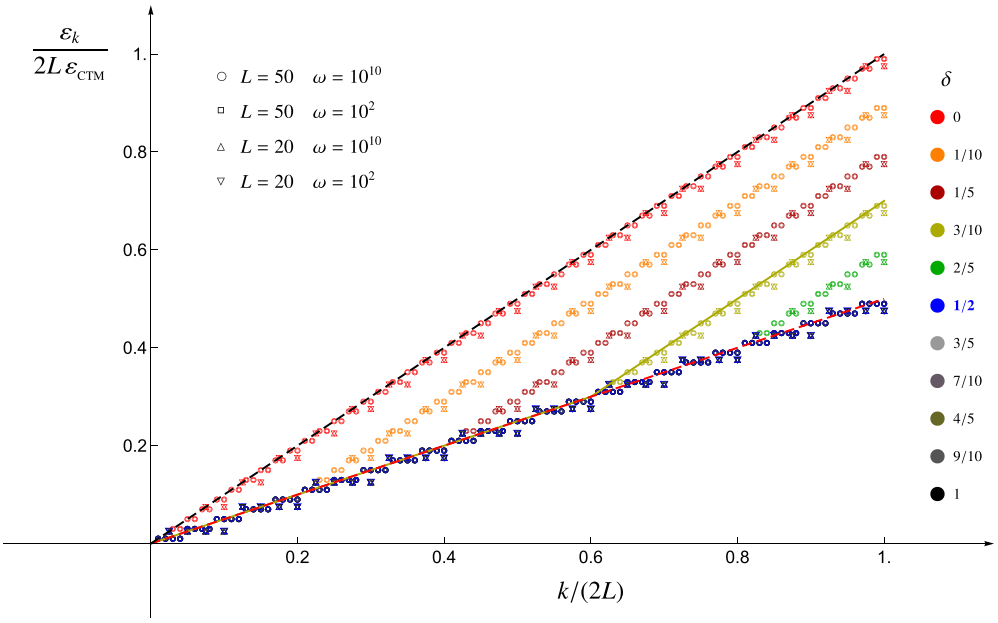

Figure 5. Single-particle entanglement spectrum for two equal blocks in the regime of large ω for various values of δ and in the same setup as figure 4. The solid yellow curve corresponds to the analytic expression in (5.13)–(5.15). The critical value of δ is (5.6), like in figure 4.

with $\eta_{\rm c}(\delta)$ being defined through the critical value $\delta_{\rm c}$ in (5.6) as

$$\eta_{\rm c}(\delta) \equiv \begin{cases} \delta/\delta_{\rm c} & \delta \leqslant \delta_{\rm c} \\ 1 & \delta > \delta_{\rm c}\,. \end{cases} \tag{5.15}$$

The results reported in figure 5 show that, in the large ω regime that we are considering, the rescaled single-particle entanglement spectrum $\varepsilon_k/(2L\,\varepsilon_{\rm CTM})$ as a function of $k/(2L)$ displays two qualitatively different behaviours for $\delta > \delta_{\rm c}$ and $\delta < \delta_{\rm c}$. First, let us remark that, as a consistency check, when $\delta = 0$, the result for the single block reported in figure 4 of [21] (bottom panel) is recovered (see the dashed black line in figure 5, whose slope is equal to 1), and in this case the degeneracy is equal to 2 because two endpoints occur. When $\delta > \delta_{\rm c}$, the rescaled single-particle entanglement spectrum is described by a straight line with a slope equal to 1/2 (see the dashed red line in figure 5), and the degeneracy of the data points along this line is equal to 4. This corresponds to the fact that, since the two blocks are independent at these separation distances, four endpoints occur at an effective level. Instead, when $\delta < \delta_{\rm c}$, the rescaled single-particle entanglement spectrum is described by a continuous piecewise linear function made by two segments having slope 1/2 for $0 < k/(2L) < \eta_{\rm c}(\delta)$ and slope 1 for $\eta_{\rm c}(\delta) < k/(2L) \leqslant 1$, where $\eta_{\rm c}(\delta)$ has been introduced in (5.15). In this phase, the degeneracy of the data points is equal to 4 for $0 < k/(2L) < \eta_{\rm c}(\delta)$ and equal to 2 for $\eta_{\rm c}(\delta) < k/(2L) \leqslant 1$. This degeneracy pattern seems to tell us that the effective number of endpoints is reduced when $\delta < \delta_{\rm c}$, becoming equal to 2 when $\delta = 0$, as expected.

https://doi.org/10.1088/1742-5468/addaa7

J. Stat. Mech. (2025) 073102

We remark that the mutual information corresponding to the single-particle entanglement spectra reported in figure 5 takes the same value for all the different values of δ, as expected from the fact that the area law holds in this regime. In particular, we have checked that the entanglement entropy of the union of two equal disjoint blocks is twice the value given by (4.11) for a single block, for all values of δ and L that we have considered. Thus, in the limit of large ω, the entanglement entropies or the mutual information cannot capture the different regimes of δ discussed above. This confirms that the entanglement Hamiltonian and its single-particle entanglement spectrum contain more information than the corresponding entanglement entropies.

6. Large ω regime: two generic blocks

In this section, the analyses performed in section 5 for two equal blocks are extended to the case where the blocks have different lengths (we can assume $L_1 \leqslant L_2$ without loss of generality); hence, the relative size of the two blocks (see (2.16)) must also be considered.

6.1. Entanglement Hamiltonian

In the regime of large ω, also for $L_1 \leqslant L_2$, we find that matrices T and V characterizing the entanglement Hamiltonian of $A = A_1 \cup A_2$ in the quadratic form (2.10) are described well by the three-diagonals approximation, discussed in section 5 for equal blocks. Our numerical analyses also show that the profiles characterizing the three non-vanishing diagonals can be conveniently written as

$$\frac{T_{i,i}}{L_A} = 2b_{\text{CTM}}\, F_2\left(\delta, \rho; \frac{i-1/2}{L_A}\right) \tag{6.1}$$

and

$$\frac{V_{i,i}}{L_A} = \left(\omega^2+2\right) 2b_{\text{CTM}}\, F_2\left(\delta, \rho; \frac{i-1/2}{L_A}\right) \qquad \frac{V_{i,i+1}}{L_A} = -2b_{\text{CTM}}\, F_2\left(\delta, \rho; \frac{i}{L_A}\right) \tag{6.2}$$

in terms of the coefficient b_{CTM} introduced in (4.3) and the function $F_2(\delta, \rho; x)$, parameterized by the dimensionless ratios (2.15) and (2.16). The special case of equal intervals, discussed in section 5, corresponds to $\rho = 1/2$. In order to write an explicit form for $F_2(\delta, \rho; x)$, let us first discuss the phases encountered for the different values of the parameters ρ and δ.

For a given value of ρ, as δ decreases from large positive values to $\delta = 0$, in our numerical analyses we have observed four different phases, which are labelled I, II, III and IV in the following (this increasing order is defined by starting from $\delta \gg 1$ and arriving at $\delta = 0$). These four phases are separated by three critical values of δ, denoted by $\delta_{\text{c}}^{\text{I/II}} > \delta_{\text{c}}^{\text{II/III}} > \delta_{\text{c}}^{\text{III/IV}}$. We find that these critical values for δ can be written in terms of the parameter ρ, as follows:

$$\delta_{\rm c}^{\rm I/II} = \frac{1}{2} \qquad \delta_{\rm c}^{\rm II/III}\,, \delta_{\rm c}^{\rm III/IV} \in \left\{ \rho\,, \frac{1}{2} - \rho \right\} \tag{6.3}$$

and the corresponding critical values $D_{\rm c}$ for the separation distance D are

$$D_{\rm c} \in \left\{ \frac{L_1 + L_2}{2}\,, \frac{L_2 - L_1}{2}\,, L_1 \right\}. \tag{6.4}$$

From (6.3), one observes the occurrence of a critical ratio $\rho = \rho_{\rm c}$ such that $\rho_{\rm c} = 1/2 - \rho_{\rm c}$, meaning that

$$\rho_{\rm c} = \frac{1}{4} \tag{6.5}$$

i.e. $L_2 = 3L_1$. When $\rho = \rho_{\rm c}$, only three phases occur because $\delta_{\rm c}^{\rm II/III} = \delta_{\rm c}^{\rm III/IV}$.

A heuristic picture explaining the critical values (6.3) has been described in section 6.3, but it would be very interesting to find them through analytic calculations.

In order to define the function $F_2(\delta, \rho; x)$ in (6.1) and (6.2), we have to introduce four piecewise linear functions with support in $x \in [a, b]$ made by a segment with a slope equal to either ± 1 or $\pm s$, with $s > 0$, written in terms of the parameters p and q satisfying $a < p < q < \frac{a+b}{2}$ when $L_1 \leqslant L_2$. In the definition of this function, the parameter $s > 0$ for the slope is kept generic for the sake of generality, but the numerical data are reproduced well for

$$s = 3. \tag{6.6}$$

It would be insightful to obtain (6.6) by employing analytic methods, *e.g.* through a derivation based on an extension of the CTM techniques.

The continuous piecewise linear functions needed to define $F_2(\delta, \rho; x)$ in (6.1) and (6.2) are

$$\bar{\Delta}\,(a, b; p; x) \equiv \begin{cases} x - a & x \in [a, p] \\ s\,x - (s-1)\,p - a & x \in [p, \tilde{p}] \\ b - x & x \in [\tilde{p}, b] \end{cases} \tag{6.7}$$

and

$$\tilde{\Delta}\,(a, b; p, q; x) \equiv \begin{cases} x - a & x \in [a, p] \\ s\,x - (s-1)\,p - a & x \in [p, q] \\ x - (s-1)\,(p-q) - a & x \in [q, \tilde{q}] \\ b - x & x \in [\tilde{q}, b] \end{cases} \tag{6.8}$$

where the parameters $\tilde{p}$ and $\tilde{q}$ read

$$\tilde{p} \equiv \frac{(s-1)\,p + a + b}{s+1} \qquad \tilde{q} \equiv \frac{(s-1)\,(p-q) + a + b}{2}. \tag{6.9}$$

J. Stat. Mech. (2025) 073102

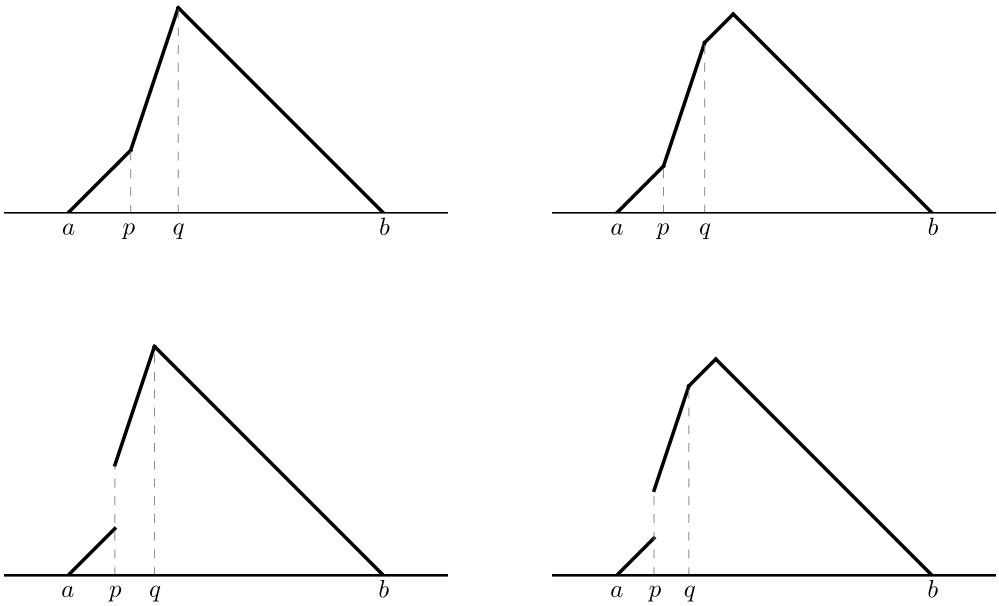

Figure 6. The auxiliary functions occurring in the definition of $F_2(\delta,\rho;x)$ (see (6.1) and (6.2)) for two generic intervals, defined in (6.6)–(6.12). The slopes of the segments in these piecewise linear functions are either ± 1 or 3.

The auxiliary functions (6.7) and (6.8) are shown in the top-left and top-right panels of figure 6, respectively. Moreover, notice that $\bar{\Delta}$ is a deformation of Δ, while $\tilde{\Delta}$ is a deformation of $\bar{\Delta}$. The other two piecewise linear functions defining $F_2(\delta,\rho;x)$ are discontinuous at $x=p$, where a finite jump of height h occurs, and are continuous at $x=q$. They read

$$\bar{\lambda}(a,b;p,h;x) \equiv \begin{cases} x-a & x\in[a,p] \\ s\,x-(s-1)\,p-a+h & x\in[p,\tilde{p}] \\ b-x & x\in[\tilde{p},b] \end{cases} \tag{6.10}$$

and

$$\tilde{\lambda}(a,b;p,h,q;x) \equiv \begin{cases} x-a & x\in[a,p] \\ s\,x-(s-1)\,p-a+h & x\in[p,q] \\ x-(s-1)\,(p-q)-a+h & x\in[q,\tilde{q}] \\ b-x & x\in[\tilde{q},b] \end{cases} \tag{6.11}$$

where the parameters $\tilde{p}$ and $\tilde{q}$ are given by

$$\tilde{p} \equiv \frac{(s-1)\,p+a+b-h}{s+1} \qquad \tilde{q} \equiv \frac{(s-1)\,(p-q)+a+b-h}{2}\,. \tag{6.12}$$

The discontinuous auxiliary functions (6.10) and (6.11) are shown in the bottom-left and bottom-right panels of figure 6, respectively. Notice that $\bar{\lambda}$ is a deformation of λ, while

J. Stat. Mech. (2025) 073102

$\tilde{\lambda}$ is a deformation of $\bar{\lambda}$. Moreover, (6.10) becomes (6.7) when $h=0$. In the following, we often enlighten the notation by adding the subindex j to the functions introduced in (6.6)–(6.12) whenever they are supported in A_j, suppressing the explicit dependence on a_j and b_j; hence, *e.g.* $\bar{\Delta}_1(p;x) \equiv \bar{\Delta}(a_1,b_1;p;x)$ and $\tilde{\lambda}_2(p,h,q;x) \equiv \tilde{\lambda}(a_2,b_2;p,h,q;x)$.

As already discussed in section 5, the choice of the parametrization of the endpoints of blocks A_1 and A_2 is crucial to perform a comparison between the analytic expression in (6.1) and (6.2) and their numerical data points. The results discussed in this section correspond to the following parametrization:

$$a_1 = -\frac{\delta}{2} - \rho \qquad b_1 = -\frac{\delta}{2} \qquad a_2 = \frac{\delta}{2} \qquad b_2 = \frac{\delta}{2} + 1 - \rho \tag{6.13}$$

meaning that A_1 and A_2 behave in the same way, symmetrically with respect to the origin, as δ decreases until $\delta=0$, where they become adjacent at the origin. Indeed, (6.13) becomes (5.9) in the special case of $\rho=1/2$, *i.e.* for $L_1=L_2$.

Instead, in appendix A, a parametrization where the endpoints of A_1 are independent of δ is considered. In particular, we use

$$a_1 = -\rho \qquad b_1 = 0 \qquad a_2 = \delta \qquad b_2 = \delta + 1 - \rho \tag{6.14}$$

meaning that, when $\delta=0$, the origin corresponds to the shared endpoint of the two adjacent blocks.

We find it worth providing further details about the construction of the function $F_2(\delta,\rho;x)$ in (6.1) and (6.2) by introducing the following rhombi, which correspond to the dashed magenta and dashed black segments in figure 7, whose slopes are $\pm 1/2$ and $2/3$, respectively. Without loss of generality, we consider the parametrization (6.13), where the origin $O \equiv (0,0)$ is fixed at the point where the two blocks join when their separation distance vanishes. Consider the rhombus $\mathcal{R}_0$ having vertices O, P_0 and $P_\pm$, where

$$P_0 \equiv (0\,,\rho) \qquad P_\pm \equiv (\pm\rho\,,\rho/2) \tag{6.15}$$

which is made by the contiguous dashed magenta segments in figure 7. Since $L_1 < L_2$, the other rhombus $\widetilde{\mathcal{R}}$ haas its vertices in P_0, P_+, $Q_<$ and $Q_>$, where

$$Q_< \equiv \left(\frac{3}{2}(1/2-\rho)\,,1/2\right) \qquad Q_> \equiv \left(\rho+\frac{3}{2}(1/2-\rho)\,,\frac{1-\rho}{2}\right). \tag{6.16}$$

The segment whose endpoints are P_0 and $Q_>$ and the one having its endpoints in P_+ and $Q_<$ have slopes equal to $2/3$ (see the dashed black segments in figure 7), while the slope of the other two segments of $\widetilde{\mathcal{R}}$ is $-1/2$. In the special case of $L_1=L_2$, *i.e.* for $\rho=1/2$, we have $Q_<=P_0$ and $Q_>=P_+$; hence, only $\mathcal{R}_0$ occurs because $\widetilde{\mathcal{R}}$ shrinks to a segment (see figure 4).

As for the parametrization (6.14), the corresponding rhombi are described in appendix A.

In figure 7, we show that, in order to define $F_2(\delta,\rho;x)$ in (6.1) and (6.2), the vertices of the auxiliary functions in figure 6 must belong to the edges of the rhombi $\mathcal{R}_0$ and

J. Stat. Mech. (2025) 073102

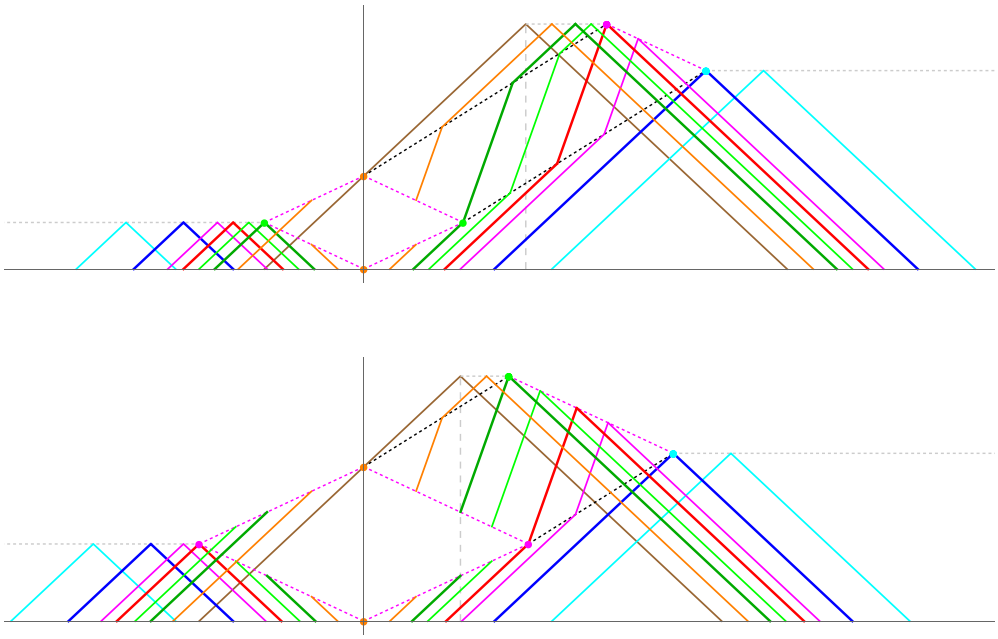

Figure 7. The function $F_2(\delta,\rho;x)$ for $\rho<\rho_c$ (top panel) and $\rho>\rho_c$ (bottom panel), given in (6.17) and (6.18), respectively, for various values of δ corresponding to different colours. Four phases occur, and each of them is described by one of the auxiliary functions shown in figure 6. The dots denote the points in (6.15) and (6.16).

$\widetilde{\mathcal{R}}$ introduced above, and to the horizontal dashed grey half lines. These constraints allow us to determine the parameters in the auxiliary functions (6.6)–(6.12), and this provides the following analytic expressions for the function $F_2(\delta,\rho;x)$ occurring in (6.1) and (6.2), which hold for the parametrization of the endpoints of A given by (6.13).

For $\rho\in\big(0,\rho_c\big]$, the function $F_2(\delta,\rho;x)$ can be written as follows:

$$F_2(\delta,\rho;x)\equiv\begin{cases}\Delta_1(x)+\Delta_2(x) & \delta\in\big[\delta_c^{\mathrm{I/II}},+\infty\big)\\ \Delta_1(x)+\bar{\Delta}_2(3a_2-\rho/2;x) & \delta\in\big[\delta_c^{\mathrm{II/III}},\delta_c^{\mathrm{I/II}}\big]\\ \Delta_1(x)+\tilde{\Delta}_2(3a_2-\rho/2,3a_2;x) & \delta\in\big[\delta_c^{\mathrm{III/IV}},\delta_c^{\mathrm{II/III}}\big]\\ \lambda_1(2b_1;x)+\tilde{\lambda}_2(2a_2,\rho-2a_2,3a_2;x) & \delta\in\big[0,\delta_c^{\mathrm{III/IV}}\big]\end{cases}\tag{6.17}$$

while for $\rho\in\big[\rho_c,1/2\big]$ it is given by

$$F_2(\delta,\rho;x)\equiv\begin{cases}\Delta_1(x)+\Delta_2(x) & \delta\in\big[\delta_c^{\mathrm{I/II}},+\infty\big)\\ \Delta_1(x)+\bar{\Delta}_2(3a_2-\rho/2;x) & \delta\in\big[\delta_c^{\mathrm{II/III}},\delta_c^{\mathrm{I/II}}\big]\\ \lambda_1(2b_1;x)+\bar{\lambda}_2(2a_2,\rho-2a_2;x) & \delta\in\big[\delta_c^{\mathrm{III/IV}},\delta_c^{\mathrm{II/III}}\big]\\ \lambda_1(2b_1;x)+\tilde{\lambda}_2(2a_2,\rho-2a_2,3a_2;x) & \delta\in\big[0,\delta_c^{\mathrm{III/IV}}\big]\end{cases}\tag{6.18}$$

https://doi.org/10.1088/1742-5468/addaa7

J. Stat. Mech. (2025) 073102

in terms of the auxiliary functions introduced in (6.6)–(6.12) and of the occurrence of the four phases I, II, III and IV, which are separated by the critical values of δ defined in (6.3).

When $\rho < \rho_c$, the function $F_2(\delta, \rho; x)$ is discontinuous only in phase IV, while for $\rho > \rho_c$ it is discontinuous in both phases III and IV. The expressions (6.17) and (6.18) provide the piecewise linear curves in the top and bottom panels of figure 7, respectively.

In the limit of either vanishing or large separation distances between the blocks, the function $F_2(\delta, \rho; x)$ defined in (6.17) and (6.18) satisfies, respectively, the following consistency conditions:

$$\lim_{\delta \to 0} F_2(\delta, \rho; x) = \Delta(-\rho, 1-\rho; x) \tag{6.19}$$

$$\lim_{\delta \to +\infty} F_2(\delta, \rho; x) = \Delta(a_1, b_1; x) + \Delta(a_2, b_2; x) \tag{6.20}$$

which become the ones in (5.10) in the special case of equal intervals, as expected.

In appendix A, we report the definition of the function $F_2(\delta, \rho; x)$ for the parametrization of the endpoints of A given by (6.14). Notice that the consistency conditions (6.19) and (6.20) also hold for this choice.

In figure 8 and figure 9, we report our numerical results for the main diagonal of matrix T in (2.10), evaluated through (2.12), in the regime of large ω and for $L_1 < L_2$. The data points are described well by the analytic expression given by (6.1), (6.17) and (6.18). In particular, these numerical results have been obtained for $\omega = 10^{10}$ by setting either $L_2 = 2L_1$ or $L_2 = 4L_1$ (top and bottom panels of figure 8, respectively) or $L_2 = 3L_1$ (figure 9, which corresponds to the critical value (6.5) for ρ). The numerical values for the critical values for δ (see (6.3)) have been highlighted through coloured and bold numbers in the legends of figures 8 and 9, and the corresponding markers in the plots have been made more visible. In the same setup, we have checked that the corresponding numerical results for the matrix V in (2.10), evaluated through (2.11), are described well by (6.2), (6.17) and (6.18), but the outcomes of these analyses have not been reported here because basically the same curves shown in figures 8 and 9 were found.

The (large) numerical values of ω have been chosen by requiring reliable collapses for the data points. In the inset in the bottom panel of figure 8, we show that, while data collapses are observed for $\delta \geqslant 1/2$ already at $\omega = 10$, for smaller separation distances, this is not the case; hence, a larger value of ω is needed to find the profiles described above. Unfortunately, larger values of ω require higher numerical precision. For instance, at $\omega = 10^{10}$, about 10^4 digits of precision are needed to obtain reliable data points.

6.2. Single-particle entanglement spectrum

The single-particle entanglement spectrum is obtained from the symplectic spectrum of γ_A through (2.14); hence, it contains less information than the entanglement Hamiltonian. In the following, this quantity is explored in the case where $L_1 \leqslant L_2$, extending the corresponding analysis performed in section 5 for two equal blocks.

J. Stat. Mech. (2025) 073102

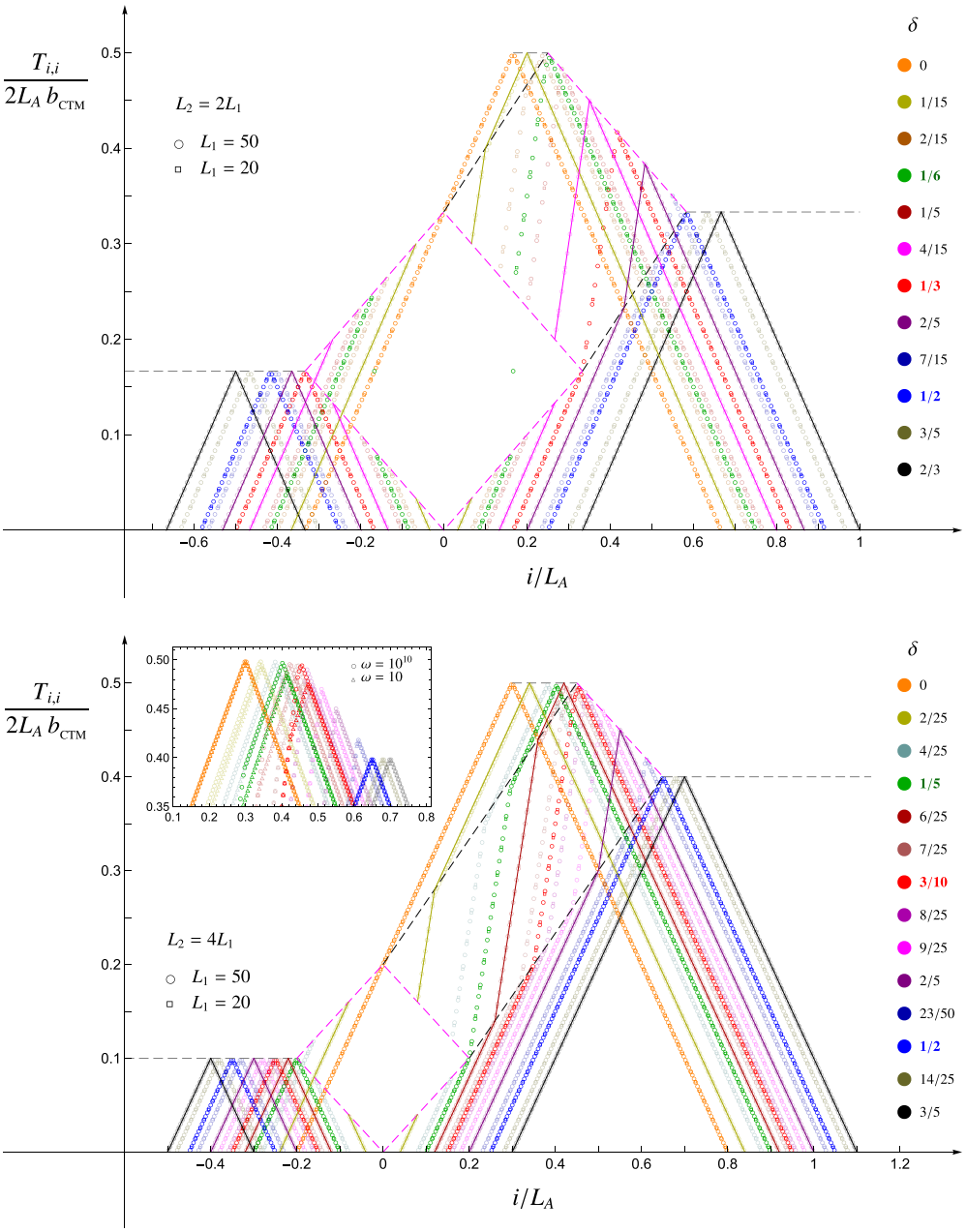

Figure 8. The main diagonal of T for two generic blocks when $\omega = 10^{10}$ for various values of δ. The solid curves correspond to (6.1). Here, $\rho = 1/3$ (top) and $\rho = 1/5$ (bottom); hence, (6.17) and (6.18) are used, respectively, for the analytic prediction (see also figure 7). The critical values (6.3) are coloured in the legend.

In the regime of large ω, our numerical results are reported in figures 10 and 11, showing the single-particle entanglement spectra for the entanglement Hamiltonians employed in figures 8 and 9, respectively. These data points in the regime of large ω are described well by

J. Stat. Mech. (2025) 073102

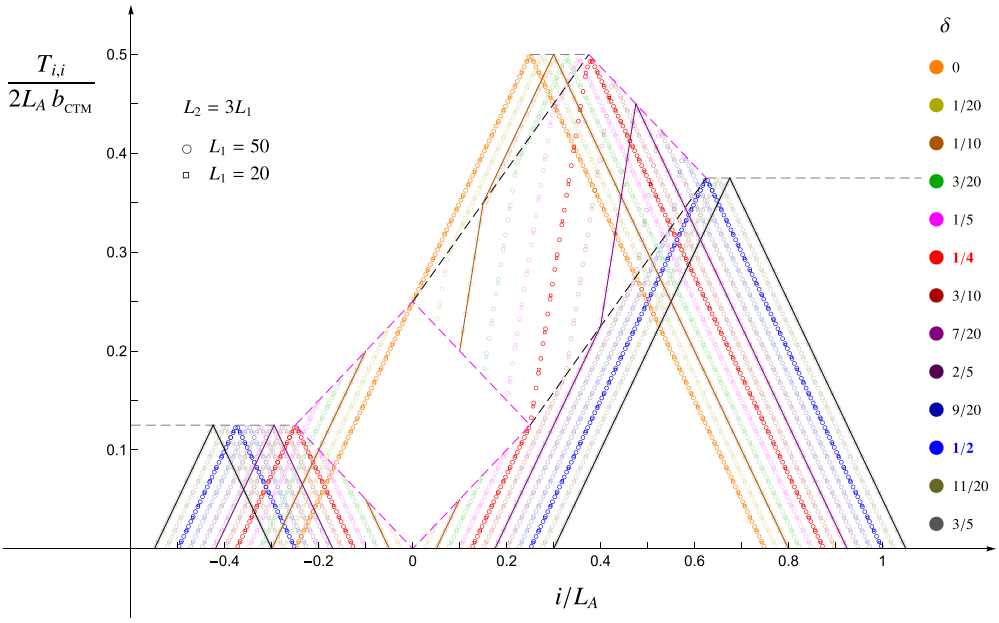

Figure 9. The main diagonal of T for two generic blocks for $\omega = 10^{10}$ and various values of δ. The solid curves correspond to (6.1), (6.17) and (6.18). Here, $\rho = \rho_{\rm c} = 1/4$ takes the critical value (6.5); hence, only three phases occur.

$$\frac{\varepsilon_k}{L_A} = \varepsilon_{\rm CTM}\, f_2\!\left(\rho, \delta\,; \frac{k}{L_A}\right) \tag{6.21}$$

where $1 \leqslant k \leqslant L_A$, the coefficient $\varepsilon_{\rm CTM}$ is (4.4) and $f_2(\rho,\delta;\eta)$ is the continuous piecewise linear function defined as follows:

$$f_2\,(\rho,\delta;\eta) \equiv \begin{cases} g_2\,(\rho,\delta;\eta) & \delta \leqslant \rho \\ g_2\,(\delta,\rho;\eta) & \delta \geqslant \rho \end{cases} \qquad \eta \in [0,1] \tag{6.22}$$

in terms of

$$g_2\,(\rho,\delta;\eta) \equiv \begin{cases} \eta/2 & \eta \in [0\,,2\delta\,] \\ \eta - \delta & \eta \in [2\delta\,,2\rho] \\ 3\eta/2 - \delta - \rho & \eta \in \big[2\rho\,, \min\big\{2\,(\rho+\delta)\,,1\big\}\big] \\ \eta & \eta \in [2\,(\rho+\delta)\,,1\,] \end{cases} \tag{6.23}$$

where the fourth segment, given by η, does not occur whenever $2(\rho+\delta) \geqslant 1$, *i.e.* for $\delta \geqslant 1/2 - \rho$. As a consistency check for (6.22), we observe that (5.14) is recovered in the special case of equal intervals, namely

$$f_2\,(1/2,\delta;\eta) = \tilde{f}_2\,(\delta;\eta)\,. \tag{6.24}$$

In figure 10, we show the single-particle entanglement spectra (rescaled through $\varepsilon_{\rm CTM}$ in (4.4), as suggested by (6.21)) corresponding to the entanglement Hamiltonians

J. Stat. Mech. (2025) 073102

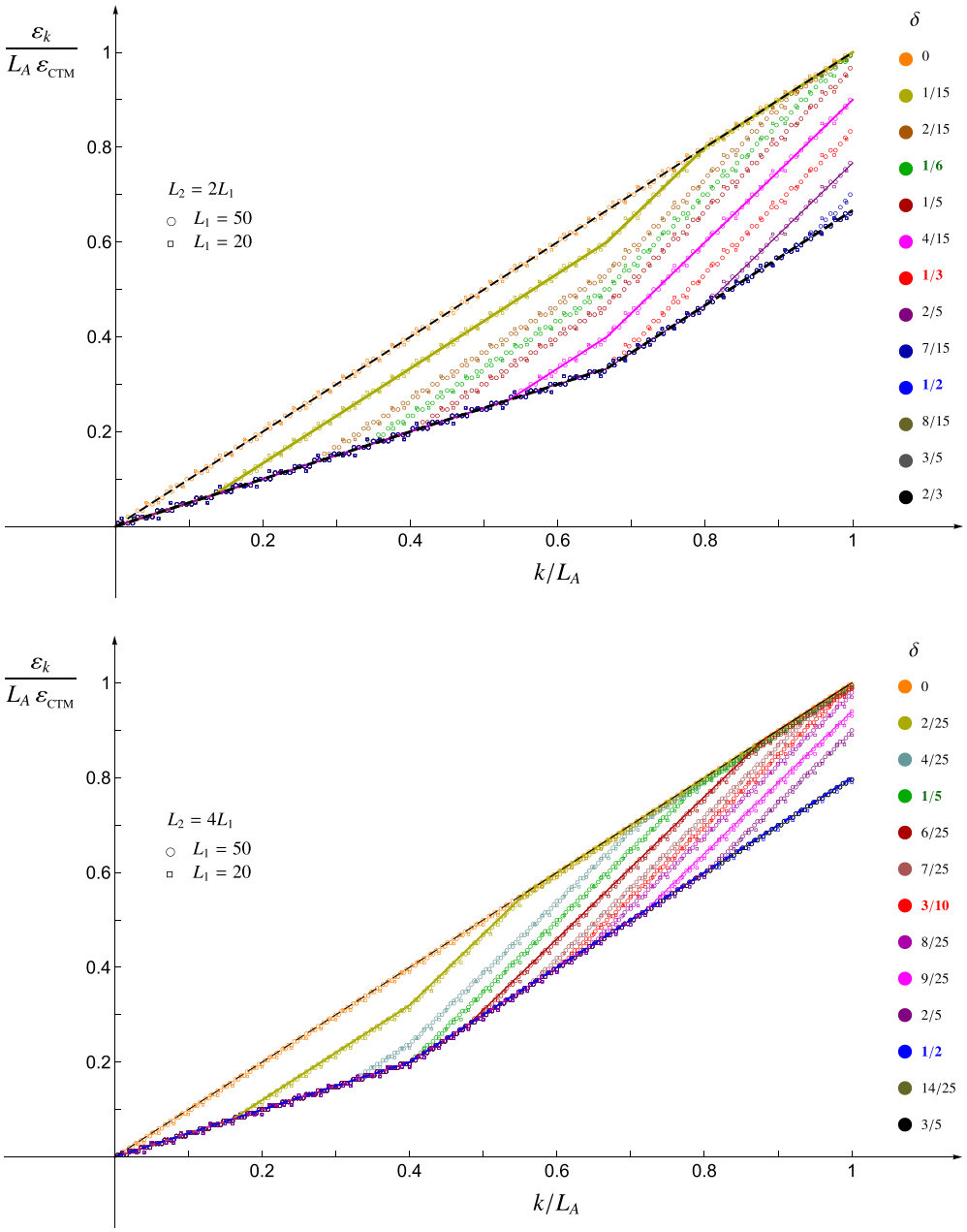

Figure 10. Single-particle entanglement spectrum for $\rho = 1/3$ (top) and $\rho = 1/5$ (bottom) in the regime of large ω and for various values of δ, in the same setup as the corresponding panels of figure 8 . The solid curves are obtained from the analytic expressions defined in (6.21)–(6.23). The critical values (6.3) are coloured in the legend.

considered in figure 8. Since $\rho = 1/3$ and $\rho = 1/5$ in the top and bottom panels, respectively, the three critical values for δ in (6.3) are distinct, and in the legend their values are bold and coloured. The numerical data points are nicely described by the analytic expressions defined in (6.21)–(6.23), as shown by the solid lines in figure 10. In figure 11,

J. Stat. Mech. (2025) 073102

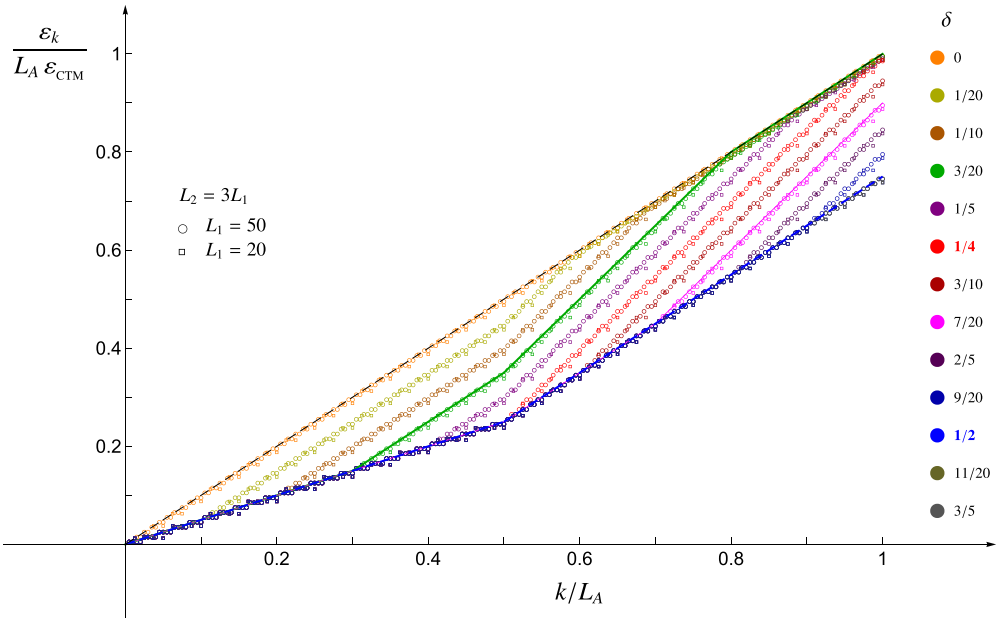

Figure 11. Single-particle entanglement spectrum for two blocks at the critical value $\rho = \rho_c = 1/4$ (see (6.5)) in the regime of large ω and for various values of δ, in the same setup as figure 9. The solid curves are obtained from the analytic expressions defined in (6.21)–(6.23).

the single-particle entanglement spectra of the entanglement Hamiltonians in figure 9 are reported, and, since $\rho = \rho_c = 1/4$ takes the critical value (6.5) in this case, only two distinct critical values of δ occur (see the coloured and bold values of δ in the legend). Different degeneracies are observed in the domains of k/L_A where the linear behaviour of the single-particle entanglement spectrum follows different slopes. In particular, the data points following slopes 1/2 and 1 have degeneracy equal to 4 and 2, respectively, while along the segments with slope 3/2, an unusual degeneracy pattern occurs.

The mutual information of two blocks for a given value of ρ does not change with their separation distance because the area law holds in this regime of large ω, similar to the equal blocks case discussed in the last paragraph of section 5.2. Moreover, also for disjoint blocks of unequal sizes, the entanglement entropy of their union is twice the value given by (4.11) for a single block, and therefore it is independent of δ, L_1 and L_2, as expected from the area law. This tells us that the various regimes for δ observed for large ω through the entanglement Hamiltonian and its single-particle entanglement spectrum cannot be captured by employing entanglement entropies, as already remarked in section 5.2.

6.3. A heuristic picture for the transitions

In the regime of large ω, the three-diagonals approximation for matrices T and V in (2.10) holds, even when subsystem A is the union of disjoint blocks, as discussed in section 5 and section 6, for $L_1 = L_2$ and $L_1 \leqslant L_2$, respectively. Here, we describe a simple heuristic geometric picture that provides the three critical values (6.4) (see also (6.3),

J. Stat. Mech. (2025) 073102

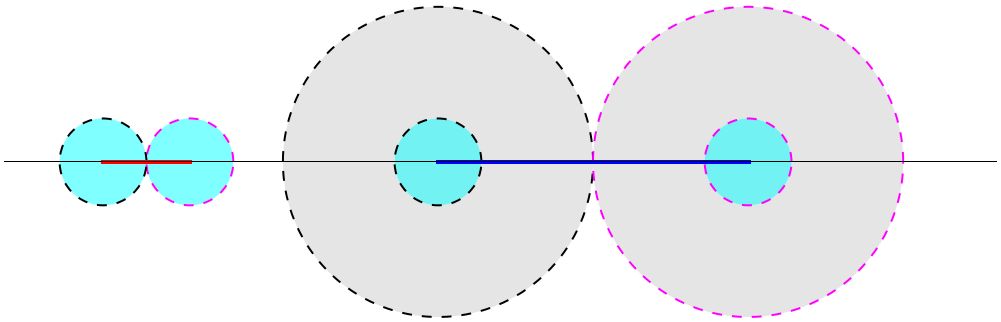

Figure 12. Configuration of disks in the heuristic picture providing the critical distances (6.4), described in section 6.3.

in terms of (2.15) and (2.16)) observed for the separation distance D between the two blocks.

In this heuristic picture, the two endpoints of each interval play different roles, as also suggested by the twist fields method [32, 58], where the entanglement entropies of the bipartition of the line associated with N disjoint intervals is computed as the $2N$-point function of twist fields, and the endpoints of each interval support different (although related) kinds of fields (for a massless regime, also see *e.g.* [35–37]). In the following, for the sake of simplicity, we focus on the case where the subsystem $A = A_1 \cup A_2$ is the union of two disjoint intervals A_1 and A_2 (*i.e.* $N = 2$) whose lengths are L_1 and L_2, respectively, where $L_1 \leqslant L_2$ without loss of generality (see the red and blue segments in figure 12).

For each endpoint of the interval $A_j = [a_j, b_j]$, with $j \in \{1,2\}$, consider a one-dimensional domain of influence of length $L_j = b_j - a_j$ centred in the endpoint itself; hence, two such domains of influence occur for the interval A_j, centred in a_j and b_j. Since these two domains are of different types, depending on whether they are centred either in the first or the second endpoint of the interval, let us denote them by $\mathcal{D}_j^+(a_j)$ and $\mathcal{D}_j^-(b_j)$, respectively, where the argument indicates the centre of the corresponding domain of influence. While for $L_1 = L_2$, only the four domains of influence $\mathcal{D}_1^+(a_1)$, $\mathcal{D}_1^-(b_1)$, $\mathcal{D}_2^+(a_2)$ and $\mathcal{D}_2^-(b_2)$ occur, when $L_1 < L_2$, besides these four domains of influence, it is natural to also introduce $\mathcal{D}_1^+(a_2)$ and $\mathcal{D}_1^-(b_2)$, with length L_1, but centred in a_2 and b_2, respectively. The six different domains $\mathcal{D}_j^\pm(y)$ mentioned above for $L_1 < L_2$ can be obtained by drawinga circle for each of them centred in the corresponding endpoint y with radius $L_j/2$. In figure 12, we show these six circles in a typical configuration, where the black and magenta dashed lines correspond to $\mathcal{D}^+$ and $\mathcal{D}^-$ types of domain, respectively. Thus, in this heuristic geometric picture, the largest interval detects the occurrence of the smallest one because its endpoints support the centres of two domains of influence of the same type but with different radii.

When $D > (L_1 + L_2)/2$, the above-mentioned disks do not intersect, but their intersections become non-trivial for $D \leqslant (L_1 + L_2)/2$. It is not difficult to realize that the

J. Stat. Mech. (2025) 073102

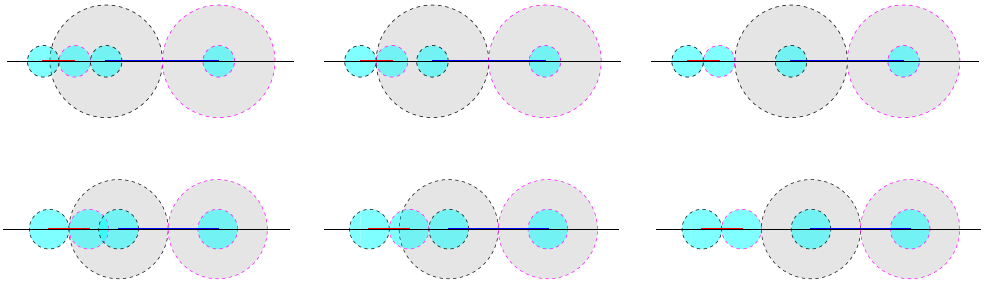

Figure 13. Configurations corresponding to the critical distances (6.4) and their disks in the heuristic picture discussed in section 6.3, for $\rho < \rho_c$ (top panels) and $\rho > \rho_c$ (bottom panels). In each row, the distance decreases from the rightmost to the leftmost panel.

critical values (6.4) correspond to the values of D where the number of intersections between the circles of different types changes.

This simple geometric criterion is illustrated in figure 13, where $\rho < \rho_c$ and $\rho > \rho_c$ (namely $L_1 < (L_2 - L_1)/2$ and $L_1 > (L_2 - L_1)/2$, respectively) in the top and bottom panels, respectively, with ρ_c being the critical value for ρ defined in (6.5). In each line of figure 13, the three panels display the three configurations of disks corresponding to the critical separation distances in (6.4), ordered in an increasing way, going from left to right.

7. Massless regime: two generic blocks

In this section, we explore the entanglement Hamiltonian of the union of two disjoint blocks $A = A_1 \cup A_2$ in the massless regime of the infinite harmonic chain.

While in the large ω regime, matrices T and V providing $\widehat{K}_A$ through (2.10) become diagonal and tridiagonal, respectively (see sections 5 and 6), in the opposite limit of vanishing mass we observe that all the matrix elements of T and V are non-vanishing; hence, in this limiting regime, $\widehat{K}_A$ becomes a genuine long-range and inhomogeneous quadratic operator. The occurrence of the zero mode, associated with the translation invariance, does not allow us to set $\omega = 0$ (see also section 2). In figure 14, we show matrices T (left panels) and V (right panels) when $\omega = 10^{-500}$, and the bipartition of the line is given by the union of the blocks A_1 and A_2 containing $L_1 = 50$ and $L_2 = 150$ sites, respectively, separated by either $D = 50$ (top panels), $D = 100$ (middle panels) or $D = 200$ (bottom panels) contiguous sites.

In the left panels of figure 14, the main diagonal and the two next to it (*i.e.* three diagonals in total) of matrix T have been removed, in order to make visible the remaining elements of the matrix, as is also done in figure 1. It is instructive to compare the top panels of figure 14 with all the panels in figure 1 because the same setup has been considered, except for the value of ω. Hence, this comparison allows us to gain insights into the massive regime by visualizing the elements of T and V that vanish as ω increases until the regime where the tridiagonal approximation starts to hold.

J. Stat. Mech. (2025) 073102

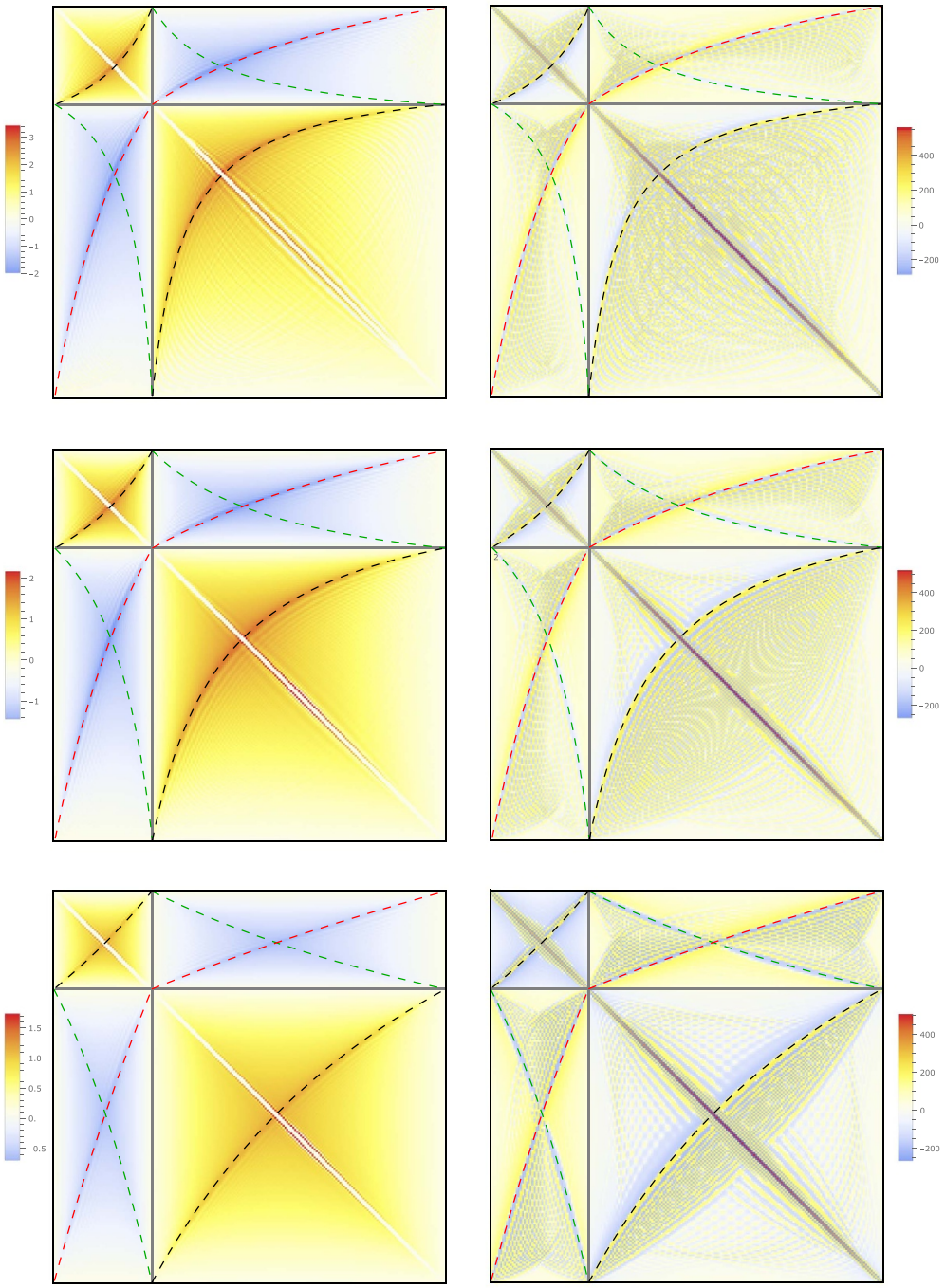

Figure 14. Matrices T (left) and V (right) in a massless regime ($\omega = 10^{-500}$) for $L_2 = 3L_1$ with $L_1 = 50$, and separation is given by $\delta = 1/4$ (top), $\delta = 1/2$ (middle) and $\delta = 1$ (bottom).

J. Stat. Mech. (2025) 073102

The block decomposition in (3.1) leads us to write the entanglement Hamiltonian (2.10) as the following sum of two quadratic operators:

$$\widehat{K}_A = \widehat{K}_{A,\mathrm{diag}} + \widehat{K}_{A,\mathrm{off}} \tag{7.1}$$

where $\widehat{K}_{A,\mathrm{diag}}$ comes from the diagonal blocks of T and V and reads

$$\widehat{K}_{A,\mathrm{diag}} = \sum_{r=1}^{2} \widehat{K}_{A_r,\mathrm{diag}} \qquad \widehat{K}_{A_r,\mathrm{diag}} \equiv \frac{1}{2} \sum_{i,j \in A_r} \left(T^{(r,r)}_{i,j} \hat{p}_i \, \hat{p}_j + V^{(r,r)}_{i,j} \hat{q}_i \, \hat{q}_j \right) \tag{7.2}$$

while $\widehat{K}_{A,\mathrm{off}}$ is provided by the off-diagonal blocks of T and V and is given by

$$\widehat{K}_{A,\mathrm{off}} = \widehat{K}^{(1,2)}_{A,\mathrm{off}} + \widehat{K}^{(2,1)}_{A,\mathrm{off}} \qquad \widehat{K}^{(m,n)}_{A,\mathrm{off}} \equiv \frac{1}{2} \sum_{\substack{i \in A_m \\ j \in A_n}} \left(T^{(m,n)}_{i,j} \hat{p}_i \, \hat{p}_j + V^{(m,n)}_{i,j} \hat{q}_i \, \hat{q}_j \right) . \tag{7.3}$$

In figure 15, we show the profiles along a given row (corresponding to the site labelled by $i = i_0$) of matrices T and V (top and bottom panels, respectively). The largest contribution comes from the main diagonal in both these matrices, which also remains non-vanishing in the opposite regime of large ω, as discussed in sections 5 and 6. By zooming in (see the insets in figure 15), one realizes that three other regions provide a significant contribution with respect to the other elements along the row. These regions are located around the intersections of the row with the curves introduced below (see (7.7), (7.9) and (7.10), which correspond to the dashed lines in figure 14), indicated by the vertical dashed segments in figure 15, with the same colour code adopted for the corresponding dashed curves in figure 14.

It is very instructive to compare figures 14 and 15 with the corresponding ones for the entanglement Hamiltonian of two disjoint blocks in an infinite fermionic hopping chain (see figures 29 and 30, respectively, where the same colour code has been adopted), whose continuum limit [23] provides the entanglement Hamiltonian for the massless Dirac free field found in [22] (these results are reviewed in appendix B for completeness). The main feature to highlight is that, in the diagonal blocks, the subleading fronts corresponding to the black dashed curves in figure 14 (whose analytic expression is given by (7.10)) do not occur in the fermionic case (see figure 29, where the same black dashed curves have been reported). In section 8 (see figures 22 and 23), we also observe the absence of this front in the free chiral current model considered in [28]. This indicates that a non-local contribution to the entanglement Hamiltonian for the massless scalar field in the continuum also comes from the diagonal blocks, in contrast to both the fermionic model and the bosonic model given by a chiral current.

It is worth considering the single-particle entanglement spectrum in a massless regime. In figure 16, we report the numerical results obtained for this quantity when $\omega L_A = 10^{-50}$ (we checked that the same values are obtained for $\omega L_A = 10^{-500}$), with either $L_2 = L_1$ (top panel) or $L_2 = 2L_1$ (bottom panel), for various values of separation distance. These results should be compared with those for the same quantities in the large ω regime, displayed in figures 5, 10 and 11. The perfect collapses of the numerical data points in figure 16 for different values of L_1 show that, in the limit $L_A \to \infty$,

J. Stat. Mech. (2025) 073102

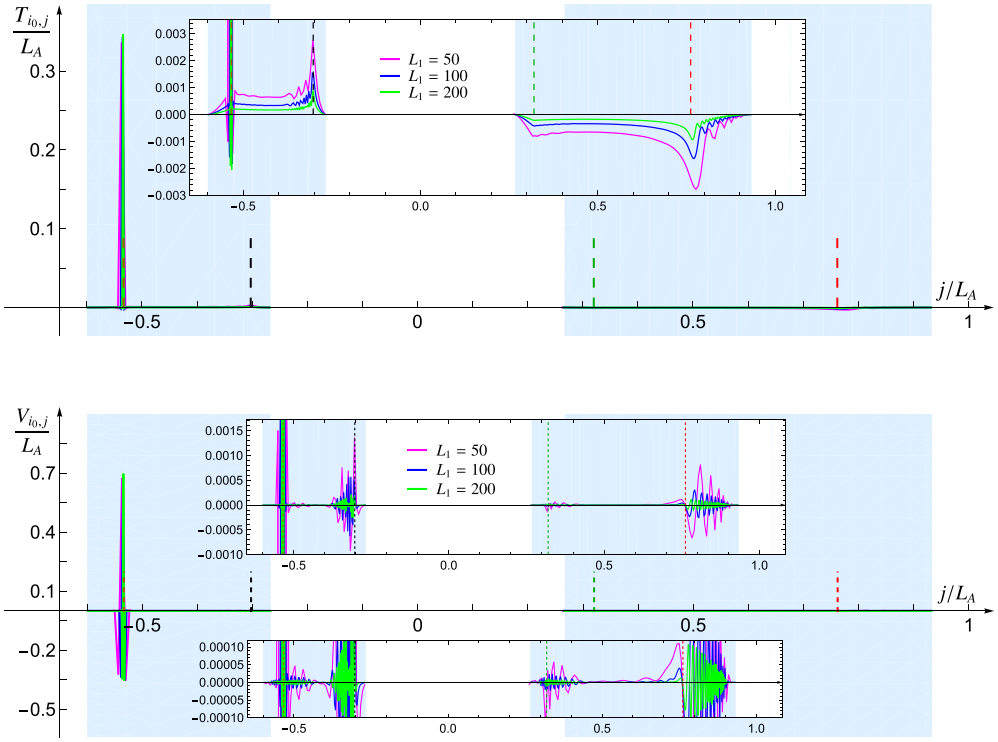

Figure 15. Matrix elements of T (top) and V (bottom) along a row corresponding to the site labelled by $i = i_0$. Here, $\omega = 10^{-500}$, $L_2 = 2L_1$, $i_0 = L_1/5$ and $\delta = 8/15$. The green, red, black and brown vertical dashed segments correspond to the intersections of the row with the curves given by (7.7), (7.9), (7.10) and the main diagonal, respectively (see also the dashed lines in figure 14). The insets zoom in to highlight the oscillatory behaviour around these particular values and their relative amplitudes.

the ratio ε_k/L_A becomes a continuous function of k/L_A parameterized by the ratios L_2/L_1 and δ. It would be interesting to obtain an analytic expression for this function. Notice that a qualitative difference occurs between the curve for $L_2 = L_1$ and the one for $L_2 = 2L_1$, namely the lack of smoothness in the latter case. This could be a footprint of $L_2 \neq L_1$.

It is important to investigate the operator coming from the continuum limit of the quadratic operators on the lattice given by (7.2) and (7.3). Previous analyses about the entanglement Hamiltonian of a single block in infinite fermionic and harmonic chains [12–15, 17] showed that it is worth considering the diagonals of matrices T and V in the thermodynamic limit. In figure 17 (left panels), we show some numerical results for the three diagonals given by $T_{i,i}$, $V_{i,i}$ and $V_{i,i+1}$, which provide the largest contributions in a massless regime and the only non-vanishing elements in a large ω regime, as discussed in sections 5 and 6. These data points have been obtained for $L_2 = 2L_1$ and $\delta = 4/30$, with $\omega L_A = 10^{-50}$, but we checked that the same results are obtained with $\omega L_A = 10^{-500}$. The nice collapses of the data sets corresponding to different values of L_1 show that the thermodynamic limit of the ratios $T_{i,i}/L_A$, $V_{i,i}/L_A$ and $V_{i,i+1}/L_A$

https://doi.org/10.1088/1742-5468/addaa7

J. Stat. Mech. (2025) 073102

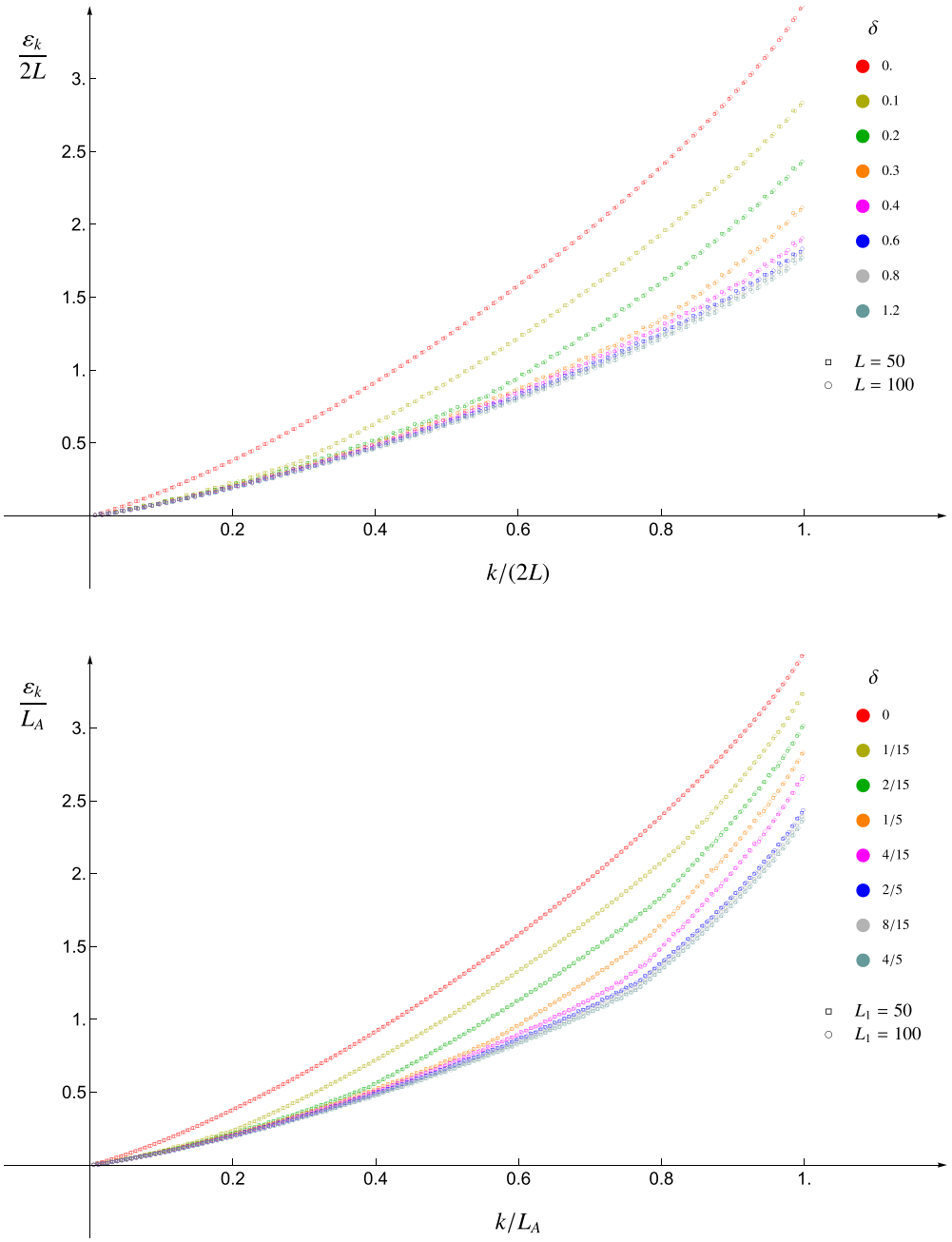

Figure 16. Single-particle entanglement spectrum in a massless regime ($\omega L_A = 10^{-50}$) when A is made by two blocks with either $L_2 = L_1$ (top) or $L_2 = 2L_1$ (bottom).

provide well-defined continuous functions, similar to the single block case [15]. In the right panels of figure 17, we show the numerical results for the discrete first derivative of the curves in the corresponding panels on the left, and the collapses of these data points tell us that the first derivative of the continuous functions coming from the thermodynamic limit of $T_{i,i}/L_A$, $V_{i,i}/L_A$ and $V_{i,i+1}/L_A$ considered in the left panels have two

spikes; hence, their second derivative is not continuous. Thus, the continuous functions in the left panels of figure 17 are not smooth, and this is in contrast with the results obtained for these quantities in the case of a single block. We remark that, in the case of an infinite harmonic chain in the ground state bipartite by a single block considered in [15], the smoothness of the functions obtained from the thermodynamic limit of the diagonals of T and V is a crucial ingredient to obtain the expected CFT result in the continuum limit (see also [16] for the sphere in higher dimensions). The lack of smoothness of the continuous functions obtained from the thermodynamic limit of the diagonals of T/L_A and V/L_A highlighted above tells us that the procedure discussed in [12, 15–17] cannot be applied straightforwardly to the case of an infinite harmonic chain in the ground state bipartite by the union of two disjoint blocks.

In appendix C, we report other numerical results about the diagonals of T/L_A and V/L_A, focusing on the special case of equal intervals for the sake of simplicity (see figures 32 and 33). The occurrence of non-smooth functions in the thermodynamic limit is also observed for higher-order diagonals.

The continuum limit of (7.2) and (7.3), where A_1 and A_2 contain L_1 and L_2 sites, respectively, and are separated by D sites, can be studied in the standard way by first introducing the lattice spacing s as the infinitesimal ultraviolet (UV) cutoff and then taking the continuum limit, namely $s \to 0^+$, $L_1 \to +\infty$, $L_2 \to +\infty$ and $D \to +\infty$ while $\ell_1 \equiv L_1\, s$, $\ell_2 \equiv L_2\, s$ and $d \equiv D\, s$ are kept fixed. In the continuum, these parameters provide, respectively, the lengths of the finite segments in the real line given by A_1, A_2 and the domain separating them. The position along the line supporting the model in the continuum is labelled $x = i\, s$, with $i \in \mathbb{Z}$ being the discrete index in (2.1), and the fields $\Phi(x)$ and $\Pi(x)$ are introduced through the operators $\hat{q}_i$ and $\hat{p}_i$ in (2.1), respectively, as

$$\hat{q}_i \;\longrightarrow\; \Phi\,(x) \qquad\qquad \hat{p}_i \;\longrightarrow\; s\,\Pi\,(x) \tag{7.4}$$

where the UV cutoff guarantees the validity of the canonical commutation relations in the continuum limit, which involve Dirac delta functions. It is convenient to rewrite the sums in (7.2) and (7.3) in the form $L_A \sum_{i\in A}(\dots) = \frac{(L_A s)}{s^2} \sum_{i\in A}(\dots) s$, which is suitable for the continuum limit (with a slight abuse of notation; here, we also denote by $A \equiv A_1 \cup A_2$ the union of two disjoint intervals A_1 and A_2 in the real line). The continuum limit $\widehat{K}_{A,\mathrm{diag}} \to K_{A,\mathrm{diag}}$ and $\widehat{K}_{A,\mathrm{off}} \to K_{A,\mathrm{off}}$ of the quadratic operators in (7.2) and (7.3), respectively, provides $K_{A,\mathrm{diag}}$ and $K_{A,\mathrm{off}}$, which are quadratic operators of the fields $\Phi(x)$ and $\Pi(x)$. It is highly non-trivial to establish whether $K_{A,\mathrm{diag}}$ and $K_{A,\mathrm{off}}$ are either local, bi-local or fully non-local operators, and it would be very interesting to find a method capable of exploring this feature.

For the sake of completeness, in appendix B we have reviewed the known results about the entanglement Hamiltonian of two disjoint intervals in the line for a massless Dirac field (which is a free fermionic CFT model with central charge $c = 1$) in its ground state [22] and its derivation from the entanglement Hamiltonian of two disjoint blocks in an infinite fermionic hopping chain at half filling through a continuum limit procedure described in [23] (see figure 31), obtained by adapting the corresponding analysis for a single block [17]. This fermionic example provides useful tools to understand some

J. Stat. Mech. (2025) 073102

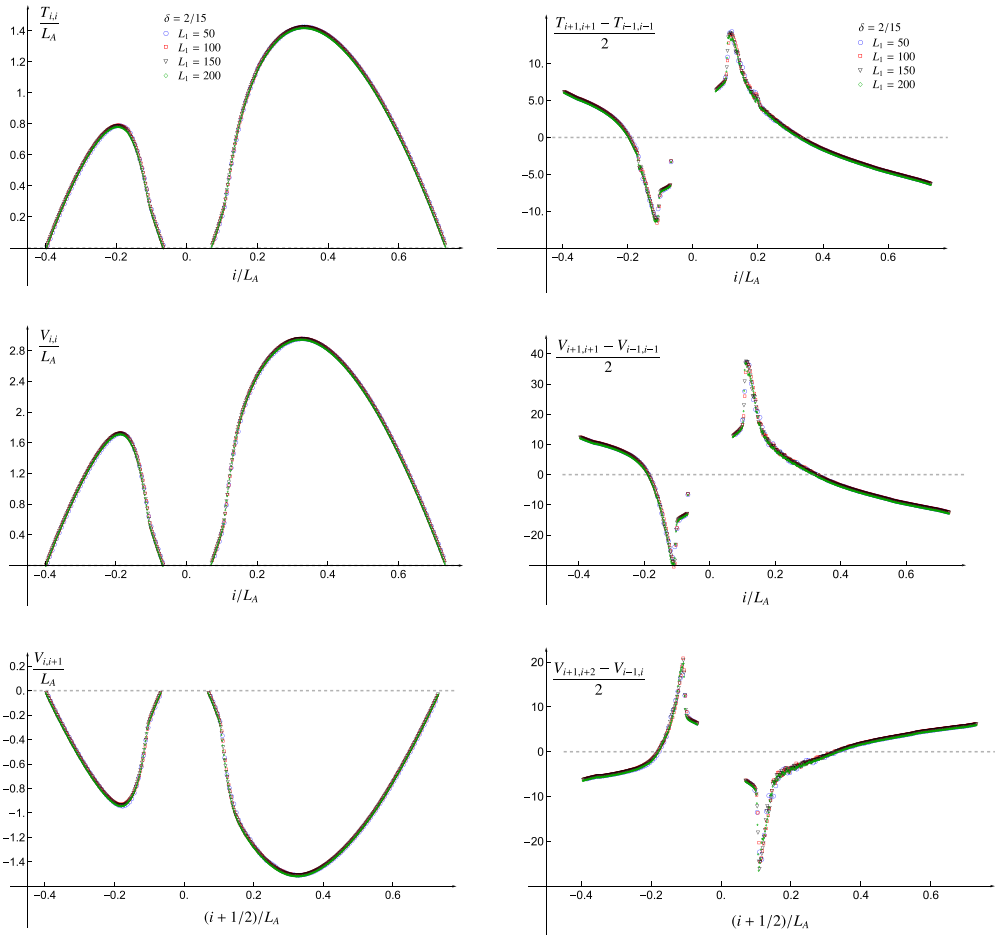

Figure 17. Diagonals $T_{i,i}$ (top left), $V_{i,i}$ (middle left) and $V_{i,i+1}$ (bottom left) for $L_2 = 2L_1$ and $\delta = 4/30$. Their discrete first derivatives are displayed in the corresponding right panels.

important features of the bosonic case explored in this section. The analytic expression of this fermionic entanglement Hamiltonian in the continuum is a quadratic operator in the Dirac field that can be written as the sum of a local term and a bi-local term [22] (see (B.1)). The local term of this entanglement Hamiltonian (see (B.2)) is given by the energy density of the massless Dirac field weighted by the following function:

$$\beta_{\rm loc}(x) = \frac{2\pi}{w'(x)} \tag{7.5}$$

where

$$w(x) \equiv \log\left(-\frac{(x-a_1)(x-a_2)}{(x-b_1)(x-b_2)}\right). \tag{7.6}$$

J. Stat. Mech. (2025) 073102

Instead, the bi-local term (see (B.4)) is a quadratic operator in the field (see (B.6)) where the two fields are evaluated in $x \in A$ and in its conjugate point $x_{\rm c} \in A$, defined as (see also [59])

$$x_{\rm c} \equiv x_0 - \frac{r_0^2}{x - x_0} \tag{7.7}$$

where

$$x_0 \equiv \frac{b_1\, b_2 - a_1\, a_2}{b_1 - a_1 + b_2 - a_2} \qquad r_0 \equiv \frac{\sqrt{(b_1 - a_1)\,(b_2 - a_2)\,(b_2 - a_1)\,(a_2 - b_1)}}{b_1 - a_1 + b_2 - a_2}\,. \tag{7.8}$$

We remark that $x_{\rm c} \in A_j$ when $x \in A_i$, with $i \neq j$.

As for the bosonic case that we are exploring in this section, the expression $x_{\rm c}$ in (7.7) as a function of $x \in A$ (obtained for the fermionic case) provides the green dashed curves in the off-diagonal blocks of the matrices displayed in figure 14.

From (7.7), let us also introduce the functions of $x \in A$ given by

$$x_{\Gamma} \equiv x_{\rm c}\big|_{a_2 \leftrightarrow b_2} = x_{\rm c}\big|_{a_1 \leftrightarrow b_1} \tag{7.9}$$

and

$$x_{\chi} \equiv x_{\rm c}\big|_{a_2 \leftrightarrow b_1} = x_{\rm c}\big|_{a_1 \leftrightarrow b_2}\,. \tag{7.10}$$

In all the matrices displayed in figure 14, the functions x_{Γ} and x_{χ} provide, respectively, the red and black dashed curves in the off-diagonal and diagonal blocks, respectively. The function x_{Γ} in (7.9) is obtained by applying the prescription proposed in [60–62] to study the negativity (a quantifier of the bipartite entanglement in mixed states obtained from the partial transposition of the reduced density matrix [63, 64]) in quantum field theory, and, in the case of a massless Dirac field in a vacuum and on the line bipartite through the union of two disjoint intervals, it occurs in the analyses of the corresponding operator [65].

The two solutions of $x_{\chi}(\tilde{x}) = \tilde{x}$ are

$$\tilde{x}_{\pm} = \frac{a_2\, b_2 - a_1\, b_1}{a_2 - a_1 + b_2 - b_1} \pm \frac{\sqrt{(a_2 - a_1)\,(b_2 - b_1)\,(b_2 - a_1)\,(a_2 - b_1)}}{a_2 - a_1 + b_2 - b_1}\,. \tag{7.11}$$

By writing the endpoints as $b_1 = a_1 + \ell_1$, $a_2 = a_1 + \ell_1 + d$ and $b_2 = a_1 + \ell_1 + d + \ell_2$, in terms of the positive parameters ℓ_1, d and ℓ_2, it is straightforward to prove that $\tilde{x}_- \in A_1$ while $\tilde{x}_+ \in A_2$. Interestingly, the expressions in (7.11) also provide the two solutions of $x_{\Gamma}(\tilde{x}) = x_{\rm c}(\tilde{x})$. This implies that, in figure 14, the intersections between the two dashed curves in the off-diagonal blocks and between the dashed curve and the main diagonal in the diagonal blocks form a square. Indeed, since one can show analytically $x_{\Gamma}(\tilde{x}_{\pm}) = \tilde{x}_{\mp}$, the four intersection points correspond to $(\tilde{x}_{\pm}, \tilde{x}_{\pm})$ and $(\tilde{x}_{\mp}, \tilde{x}_{\pm})$. In the special case of

J. Stat. Mech. (2025) 073102

the symmetric configuration $A = A_{\rm sym} = (-b,-a)\cup(a,b)$ with $0<a<b$, the expressions in (7.11) drastically simplify to

$$\tilde{x}_{\pm}\big|_{A=A_{\rm sym}} = \pm\sqrt{a\,b}\,. \tag{7.12}$$

In the continuum limit procedure for the entanglement Hamiltonian of two disjoint blocks in the infinite fermionic chain in its ground state, discussed in [23] and reviewed in appendix B, the weight function of the bi-local term given in (B.5) has been obtained by introducing a specific combination of all the elements along a line of the off-diagonal blocks (see (B.13)), finding excellent agreement (see also the right panel of figure 31). This result for the fermionic case suggests that, also for the bosonic case that we are exploring, one should consider specific combinations of all the elements along a line.

For the diagonal blocks occurring in (7.2), let us introduce

$$\mathsf{T}_{\rm diag}(i) \equiv \begin{cases} \displaystyle\sum_{j\in A_1} T_{i,j} & i\in A_1 \\ \displaystyle\sum_{j\in A_2} T_{i,j} & i\in A_2 \end{cases} \qquad \mathsf{V}_{\rm diag}(i) \equiv \begin{cases} \displaystyle\sum_{j\in A_1} V_{i,j} & i\in A_1 \\ \displaystyle\sum_{j\in A_2} V_{i,j} & i\in A_2 \end{cases} \tag{7.13}$$

and, similarly, for the off-diagonal blocks in (7.3), we define the following row-wise combinations:

$$\mathsf{T}_{\rm off}(i) \equiv \begin{cases} \displaystyle\sum_{j\in A_2} T_{i,j} & i\in A_1 \\ \displaystyle\sum_{j\in A_1} T_{i,j} & i\in A_2 \end{cases} \qquad \mathsf{V}_{\rm off}(i) \equiv \begin{cases} \displaystyle\sum_{j\in A_2} V_{i,j} & i\in A_1 \\ \displaystyle\sum_{j\in A_1} V_{i,j} & i\in A_2. \end{cases} \tag{7.14}$$

In figures 18 and 19, we show some numerical results for the combinations of elements along the ith row of T and V introduced in (7.13) and (7.14), respectively, when $L_2 = 2L_1$ and for various values of δ. Notice that these combinations scale in different ways for the two different matrices. The black dashed curves in figure 18 correspond to (7.5) occurring in the fermionic case mentioned above (see also appendix B), while the solid green curve is its limit for a large separation distance $d\to+\infty$, which is given by $2\pi\,(b_1-x)(x-a_1)/(b_1-a_1)$ when $x\in A_1$ and by $2\pi\,(b_2-x)(x-a_2)/(b_2-a_2)$ when $x\in A_2$. In each figure, the top panel shows separately the contributions of the diagonal block and the off-diagonal block for a given row, while in the bottom panel the sum of these two contributions is considered.

In the bottom panel of figure 18, the main diagonal of T is also shown. The nice collapses of the data points observed in figures 18 and 19 indicate that these combinations, once scaled in the proper way, provide well-defined functions in the thermodynamic limit. Finding the analytic expressions of these functions is an interesting problem for future studies.

As for figure 18 regarding T, the data points collapse on the weight function (7.5) near the entangling points of subsystem A, but a discrepancy with this analytic curve is observed in the central part of A_1 and A_2. When $\delta=0$, the red data points in figure 18 reproduce well the result of [15] for a single block, as expected, and from the bottom

J. Stat. Mech. (2025) 073102

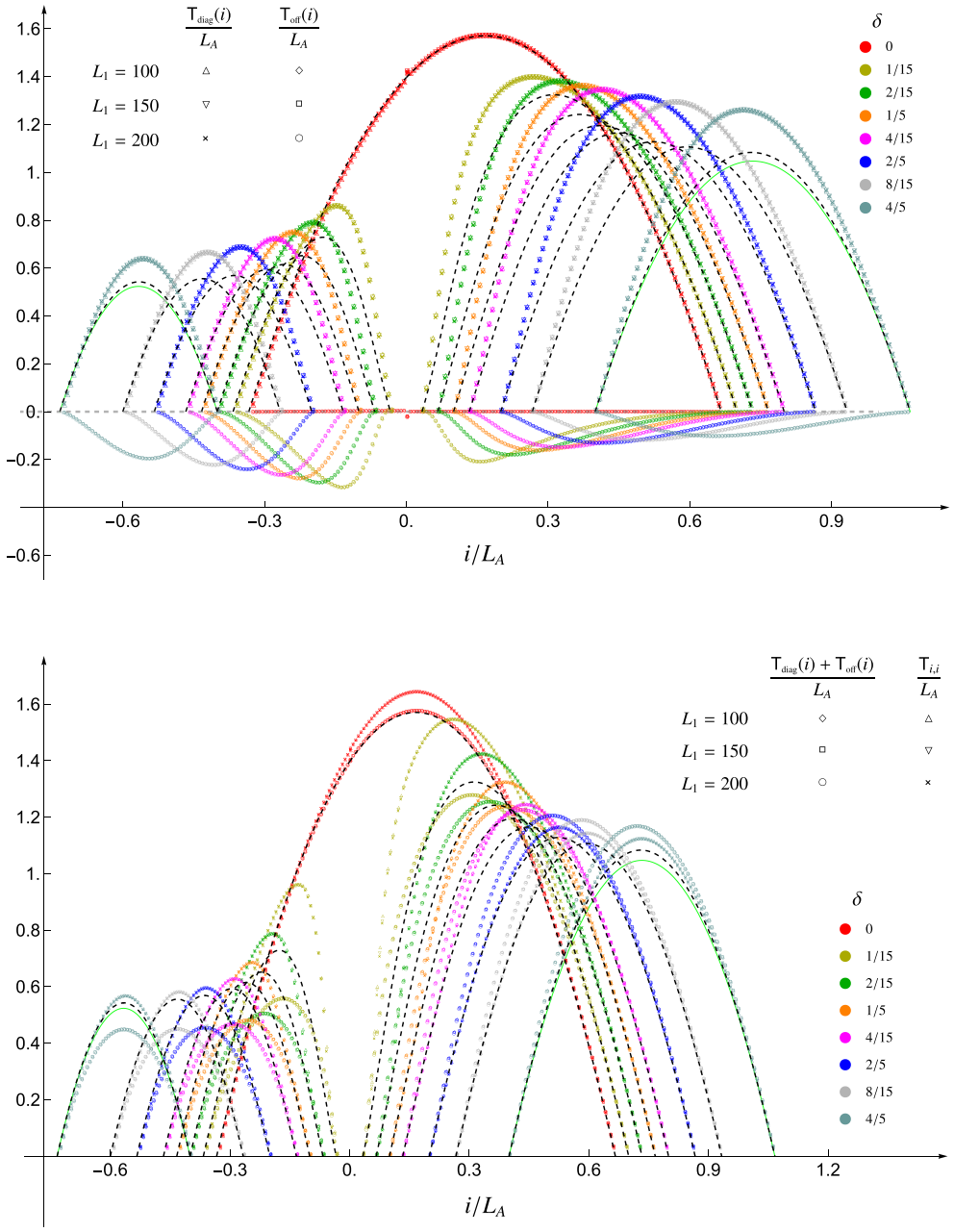

Figure 18. Combinations of elements in T defined in (7.13) and (7.14), for $L_2 = 2L_1$.

panel we see that the main diagonal of T is not enough to capture the parabolic function occurring in the continuum limit; hence, the contribution of the elements outside the main diagonal is also needed.

In figure 19, where the combinations of elements of V defined in (7.13) and (7.14) are considered, we observe that the diagonal blocks and the off-diagonal blocks provide very similar curves, except for an overall sign. However, their sum is not noisy, although two orders of magnitude smaller than each term, as shown in the bottom panel of the figure.

J. Stat. Mech. (2025) 073102